INVESTIGATION OF PETROPHYSICAL PROPERTIES

AND FLUID MIGRATION

IN UNCONVENTIONAL OIL/GAS RESERVOIRS

by

YUXIANG ZHANG

THESIS

Submitted in partial fulfilment of the requirements
for the degree of Doctor of Philosophy at
The University of Texas at Arlington
May 2019

Arlington, Texas

Supervising Committee:

Qinhong Hu, Supervising Professor
John S Wickham
Majie Fan
William Ashley Griffith
Cheng Luo

Abstract

Investigation of Petrophysical Properties and Fluid Migration in Unconventional Oil/Gas Reservoirs

Yuxiang Zhang, Ph.D.

The University of Texas at Arlington, 2019

Supervising Professor(s): Qinhong Hu

Petrophysics deals with the physical and chemical properties of petroleum-bearing rocks and their interactions with associated fluids. The investigation of petrophysical properties of interest, such as porosity, specific pore surface area, pore size distribution, permeability, fluid saturation, and wettability, is of great importance to understand hydrocarbon storage and transport in unconventional oil/gas reservoirs, especially shale reservoirs. Characterized as low-porosity and ultra-low permeability, unconventional reservoir rocks have complicated pore structure which is significantly affected by their dominant compositions (minerals and organic matters) and vary along with the depositional environment, burial depth, diagenesis, and thermal maturity. Therefore, to better understand the shale properties and their controlling factors, a combination of various laboratory-based petrophysical measurements was designed to study core samples from major U.S. and China shale plays. The techniques involved are mercury injection capillary pressure (MICP) analysis, low-pressure gas (N_2/CO_2) physisorption, scanning electron microscopy (SEM) imaging, and as a major focus of this dissertation, the small- and ultra-small-

angle neutron scattering (SANS and USANS) techniques. Assisted with geochemical analyses of X-ray diffraction, pyrolysis, and total organic carbon content, the combined petrophysical studies depict a more comprehensive picture of the multiscale pore structure across the nm-μm spectrum. In addition, the application of a contrast matching technique in SANS/USANS measurement allows the differentiation of wettability to various fluids and quantification of their volume at multiple scales, which has guiding importance to the recoverable volume of oil and gas. In general, this study shows a comprehensive petrophysical study of several shale samples and provides valuable insight for predicting and optimizing oil and gas production.

Acknowledgements

I would first like to thank my dissertation advisor Dr. Qinhong Hu of the Department of Earth and Environmental Sciences at the University of Texas at Arlington. He offered me the opportunity to continue my education in the United States and instructed me to be a scientific researcher in petroleum geosciences. Thanks to him, I was able to get access to invaluable resources, gain hands-on experience and expand scientific knowledge, and eventually succeed in my doctoral research.

Special thanks to Troy Barber who led me into the field of neutron research in geosciences and worked with me to make neutron experiments successful. I would also like to thank Dr. Markus Bleuel of NIST Center for Neutron Research who helped me a lot in experiments preparation and data processing. Without them, a significant portion of my research work cannot be completed.

I would like to acknowledge all my professors at UTA for teaching me and helping me in the past five years. Thanks to Dr. John Wickham, Dr. William Griffith, Dr. Majie Fan, and Dr. Cheng Luo for guiding me in academic research. I am also thankful to my career advisors William Moulton and Wayne Hoskins for help me building up my networks and providing me with career suggestions.

I am very grateful to all my colleagues in the department, and it was great studying and working with them. I am also deeply thankful to my friends in Arlington, especially my roommate Zijian Li, who gave me great support and assistance during my daily life.

April 23, 2019

Dedication

This dissertation is dedicated to my parents, my family members, and my girlfriend. Their unfailing support, encouragement, and love have sustained me throughout my student's life.

Table of Contents

Chapter 1: Introduction

The shale revolution has been significantly stimulating oil and gas production in North America, thanks to advances in horizontal drilling and hydraulic fracturing techniques, and making the United States energy independent. However, most shale wells encounter a sharp production decline after hydraulic fracturing or re-fracking in the first several years. Contrary to conventional petroleum reservoirs (sandstone and carbonates), the storage and migration mechanisms responsible for hydrocarbon transport in the complex, heterogeneous matrices of tight shale reservoirs are still poorly understood. Therefore, it is critical to have a better way for pore structure characterization in order to tease out the underlying controls on hydrocarbon production declines and provides valuable insights for predicting and optimizing the production of oil and gas.

Laboratory-based techniques for reservoir characterization include petrophysical approaches, image analyses, and scattering methods. Commonly used petrophysical analyses on rocks include saturation (or imbibition), helium (He) porosimetry, low-pressure gas (N_2 and CO_2) physisorption, and mercury injection capillary pressure (MICP). Image analyses provide a direct description of the pore size and pore types associated with the rock matrix (minerals or organic matters), especially argon ion-milled field emission-scanning electron microscopy (FE-SEM) which has been widely employed for nm-μm scale pore structure characterization. Scattering techniques use radiation (e.g., neutron, X-ray) to investigate pores in rocks and provide statistically meaningful, quantified understanding of pore structure (Anovitz and Cole, 2015). Overall, all of these techniques yield unique information about the pore structure, as they operate on different working principles and probe different aspects of pore geometry and topology. As

such, a combination of multiple and complementary methods is often necessary to gain a comprehensive understanding of the overall pore structure.

As will be discussed in the following three chapters, mercury injection capillary pressure (MICP) analysis and combined ultra-small-/small angle neutron scattering (USANS/SANS) techniques, are the two primary approaches in this work used for characterizing multiscale pore structure of shale samples.

MICP is one of the standard and powerful techniques applied to study reservoir rocks. It measures skeletal/bulk densities, porosity, pore surface area, and pore-throat size distribution directly, and can yield information of permeability and tortuosity, across a wide size range (nm-μm scale) (Webb 2001; Gao and Hu, 2015). Owing to its inherent non-wetting property, mercury can only enter the interconnected pores under a progressively increased pressure. According to the Washburn Equation (Washburn, 1921), most of the instrumentations can reach a maximum pressure of 60,000 psi (413 MPa), which yields a minimum detecting pore-throat size (diameter) of around 3 nm. The largest pore-throat diameter can be measured is 50 μm corresponding to an initiating (filling) pressure of 5 psi (0.034 MPa) for low porosity (<5%) samples, and more than 1000 μm at a filling pressure of 0.1 psi (0.69 Pa) for larger porosity samples.

SANS and USANS have been uniquely useful techniques for non-invasive investigation of rock pore structure and pore accessibility in the last two decades (Radlinski, 2006; Clarkson et al., 2012; Blach et al., 2017). Unlike MICP which in particular cannot access pores smaller than 3 nm (Clarkson et al., 2012), SANS can reach a minimum quantifiable size of 1 nm, and therefore, the combined USANS and SANS measurements can yield the assessment of porosity in a broad size spectrum from 1 nm to 20 μm. Besides, in comparison with other fluid intrusion methods which only detect surface-accessible (open) porosity, (U)SANS technique is capable of

measuring total porosity to include closed porosity. Furthermore, a very useful approach named contrast matching technique proposed by Melnichenko et al. (2012), which can be applied in (U)SANS to quantify accessible vs. inaccessible porosity to a fluid, is employed in our study and further modified to quantify oil-accessible/water-accessible porosity.

Imaging techniques directly describe the nature of pores and its association with minerals or organic matters in shales. In the following chapters, SEM imaging will serve as a primary tool for observing pore types at different scales and providing evidence for results from MICP and (U)SANS.

Overall, this dissertation will use three chapters to demonstrate the investigation of petrophysical properties of shales. Chapter 2 provides a case study for the micro- and nano-pore structure characterization of the organic-rich marine shale in the Bakken Formation (Williston Basin, U.S.) using SANS/USANS, MICP, and SEM imaging approaches. Chapter 3 uses similar methodologies to characterize saline lacustrine shales in Qianjiang Depression (Jianghan Basin, China) (Zhang et al., 2019). Chapter 4 presents the methodology of applying contrast matching technique to study fluid-accessible porosity in Utica and Bakken Shales. Chapter 5 will summarize the major findings and key points discussed in Chapter 2-4.

References

Anovitz, L.M., Cole, D.R., 2015. Characterization and analysis of porosity and pore structures, in: Reviews in Mineralogy and Geochemistry. pp. 61-164. https://doi.org/10.2138/rmg.2015.80.04

Clarkson, C.R., Solano, N., Bustin, R.M., Bustin, A.M.M., Chalmers, G.R.L., He, L., Melnichenko, Y.B., Radliński, A.P., Blach, T.P., 2013. Pore structure characterization of North American shale gas reservoirs using USANS/SANS, gas adsorption, and mercury intrusion. Fuel. v. 103, p. 606-616. https://doi.org/10.1016/j.fuel.2012.06.119

Gao, Z., and Hu, Q., 2015, Investigating the effect of median pore-throat diameter on spontaneous imbibition. Journal of Porous Media, v. 18, no. 12, p. 1231-1238, doi: 10.1615/JPorMedia.v18.i12.60.

Washburn, E.W, 1921, The dynamics of capillary flow. Physical review, v. 17, no. 3, p. 273-283, doi: 10.1103/PhysRev.17.273.

Webb, P.A., 2001. An introduction to the physical characterization of materials by mercury intrusion porosimetry with emphasis on reduction and presentation of experimental data. Micromeritics Instrument Corp, Norcross, Georgia.

Zhang, Y., Hu, Q., Long, S., Zhao, J., Peng, N., Wang, H., Lin, X., Sun, M., 2019, Mineral-controlled nm-μm-scale pore structure of saline lacustrine shale in Qianjiang Depression, Jianghan Basin, China. Marine and Petroleum Geology, v. 99, p. 347-354. https://doi.org/10.1016/j.marpetgeo.2018.10.016

Chapter 2: Complementary Neutron Scattering, Mercury Intrusion and SEM Imaging Approaches to Micro- and Nano-pore Structure Characterization of Tight Rocks: A Case Study of the Bakken Shale

Yuxiang Zhang[1], Troy J. Barber[1], Qinhong Hu[1 *], Markus Bleuel[2,3], Hesham F. El-Sobky[4]

[1] Department of Earth and Environmental Sciences, The University of Texas at Arlington, 500 Yates Street, Arlington, TX 76019, USA

[2] Center for Neutron Research, National Institute of Standards and Technology, Gaithersburg, MD 20899, USA

[3] Department of Materials Science and Engineering University of Maryland College Park, MD 20742, USA

[4] Technology and Subsurface, ConocoPhillips, Houston, TX 77079, USA

Submitted to:

International Journal of Coal Geology

[*]Corresponding author; e-mail: maxhu@uta.edu.

Abstract

Small angle neutron scattering (SANS) and ultra-small angle neutron scattering (USANS) techniques have been increasingly utilized to study tight rocks (e.g., shales) due to their capabilities of detecting total pore spaces (both body and throat) across the nm-μm spectrum. Base on pore-throat measurements, mercury injection capillary pressure (MICP) is a widely employed technique in the oil and gas industry to obtain a variety of petrophysical properties of porous rocks. In this study, we selected six shale samples from three (i.e., lower, middle, and upper) members of the Bakken Formation in Williston Basin, North Dakota, and utilized the complementary techniques of (U)SANS and MICP to characterize and differentiate their pore systems at a broad measurable range of pore/throat sizes from 1.25 nm to 50 μm. Detailed processing of (U)SANS scattering data is illustrated to show how the total porosity and pore size distribution are obtained and compared against MICP analyses. The results show that the lower/upper Bakken samples and the middle Bakken samples have distinct mineral compositions and organic matter contents which could be important factors affecting their pore structure. Assisted with the field emission-scanning electron microscopy (FE-SEM) technique, it is found that organic matter-hosted pores contribute a significant portion of total porosity in the lower/upper Bakken shales, while the middle Bakken samples are mostly composed of mineral pores. Additionally, the porosities measured by (U)SANS technique are overall larger than those obtained from MICP, due to limited pore accessibility of shale, that is related to sample sizes used in both techniques, and different detection (total vs. surface-accessible) associated with two techniques. In general, the results indicate that the combination of (U)SANS, MICP, and FE-SEM approaches gives a more complete picture of tight rock's pore structure, such as the Bakken shales demonstrated in this study.

1. Introduction

The shale revolution has been steadfastly stimulating United States' oil and gas production over the past decades, owing to advances in the techniques of horizontal drilling and hydraulic fracturing. The Bakken petroleum system is the third largest tight-oil producer in the United States, producing ~1 million barrels/day of oil, and ~2,000 million cubic feet/day of natural gas (EIA, 2018). Currently, over 98% of drilling activities in this petroleum system target the Bakken and Three Forks formations (Patterson, 2016).

In the Bakken petroleum system, apart from conventional reservoirs formed from petroleum accumulations through buoyancy, large areas of the Bakken are considered continuous petroleum accumulations as the oil and gas are charged into reservoirs including the source rocks and nearby rock formations (Nordeng, 2009). Though horizontal drilling and well stimulation create a steady oil/gas production in most of the wells, the storage and migration mechanisms responsible for hydrocarbon transport in the complex, heterogeneous matrices of tight shale reservoirs are still poorly understood for the Bakken petroleum system (e.g., Liu et al., 2017). In order to tease out the underlying controls on hydrocarbon production and more accurately forecast the production capacity of the reservoir, it is critical to have a better characterization of the hierarchical nm-μm pore architecture and effective porosity of both source and reservoir rocks.

A wide range of techniques, including petrophysical approaches, scattering methods, and image analyses, have been applied to study the pore structure (both geometry and topology, Hu et al., 2015) of tight mudrocks (e.g., Loucks et al., 2009, 2012; Passey et al., 2010; Gao et al., 2013; Anovitz and Cole, 2015; Hu et al., 2015; 2017). Operating on different working principles to probe different aspects of pore geometry and topology, each of these techniques yields unique

information about the pore structure of various scales. As such, a combination of multiple and complementary methods will be able to provide the structural information of micropores (<2 nm), mesopores (2-50 nm), and macropores (>50 nm) (pore types defined by McNaught and Wilkinson, 1997) over a broad spectrum in order to gain a comprehensive understanding of the overall pore structure characteristics.

The target of this study is the Devonian-Mississippian aged Bakken Shale. The Bakken petroleum system consists of the Bakken Formation, lower Lodgepole Formation, and upper Three Forks Formation (LeFever, 2008; Figure 1). The source rocks are the black organic-rich shales in the lower and upper members of the Bakken Formation, while the reservoir rocks encompass all three (lower, middle, and upper) Bakken members, as well as the lower Lodgepole, and upper Three Forks Formations (Sonnenberg and Pramudito, 2009). It is commonly accepted that both lower and upper Bakken members are deposited in an offshore marine environment and are lithologically similar (Pitman et al., 2001; Simenson et al., 2011), except that the upper member has a higher organic matter content while the lower member has crystallized limestone and greenish gray shale beds (Webster 1984; Pitman et al., 2001). It is reported that significant diagenetic alterations (such as cement precipitation, replacement of both detrital and authigenic minerals, and compaction etc.) happened in the organic-rich upper shale member and are at least partly responsible limiting the porosity for hydrocarbon storage (Fishman et al., 2015). With highly variable lithologies, the middle member of Bakken consists of an interbedded sequence of siltstones and sandstones with light-gray to medium-dark-gray colors (Webster 1984; LeFever et al., 1991; Pitman et al., 2001). Major diagenetic events (such as mechanical compaction, dolomitization, and dissolution of calcite and dolomite etc.) are specifically mentioned in the work of Kowalski and Sonnenberg (2011).

This article primarily focuses on introducing and discussing the integrated methodology of applying (U)SANS (ultra-small- and small-angle neutron scattering) and MICP (mercury injection capillary pressure), aided with FE-SEM (field emission scanning electron microscopy) imaging, to characterize Bakken sample's pore geometry in a broad μm-nm-scale pore length spectrum.

2. Methods and Theories

2.1 Samples and Composition Measurements

The studied samples were from two producing wells in North Dakota (Figure 1): Anderson 28-33 (API number: 33-061-00765) and Kubas (API number: 33-089-00586), to be denoted as Anderson and Kubas in the following context. Fragmented core samples (Figure 2) were supplied by the North Dakota Geological Survey (NDGS), and the well information, depths, and formations are summarized in Table 1. Three rock samples from the Anderson well belong to each member of the Bakken Formation, and thus, are termed as Anderson-U, -M and -L. Similarly, two of the Kubas samples are named Kubas-U and Kubas-M because they are from the upper and middle members, respectively. The third Kubas sample is situated at the boundary of middle and lower member where there is a sharp increase of gamma ray to indicate an entrance into the lower shale member; therefore, this sample is denoted as Kubas-M/L. Correspondingly, visual observations separate these six samples into two different sets: (1) Anderson-U, Anderson-L, and Kubas-U are all black shales; and (2) Anderson-M, Kubas-M, and Kubas-M/L are gray to dark-gray calcareous siltstone. These two sets of samples were selected as they have distinctive compositional differences, especially the organic matter (OM) contents and mineralogy for us to observe their effects on pore structure.

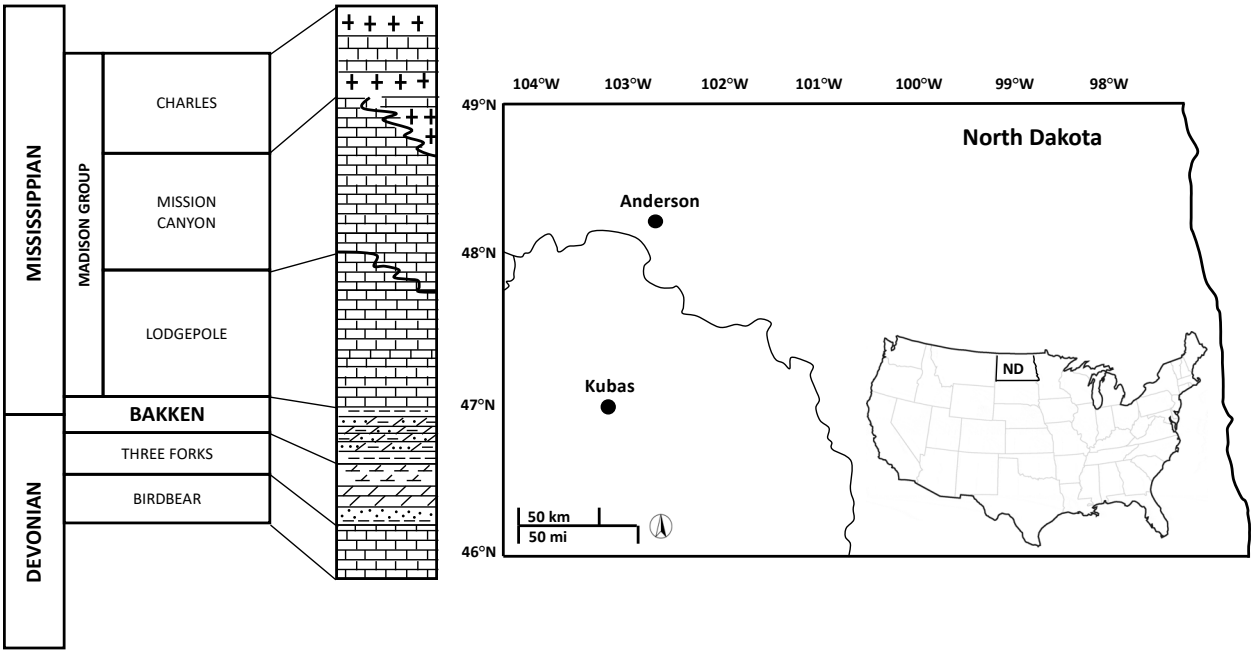

Figure 1. Stratigraphic column of the Bakken Formation (modified from Webster, 1984) and well locations of Anderson (48.23N, -102.53W) and Kubas (46.94N, -103.12W) in North Dakota.

Table 1. Information of six Bakken samples used in this study

Sample ID	Well information	Depth ft (m)	Formation
Anderson-U	Well name: Anderson 28 1-H;	10064 (3067.5)	upper Bakken member
Anderson-M	County: Mountrail;	10121 (3084.9)	middle Bakken member
Anderson-L	Operator: Brigham Oil & Gas, L.P; Field: Alger	10124 (3085.8)	lower Bakken member
Kubas-U	Well name: Kubas 11-13TFH;	10626 (3238.8)	upper Bakken member
Kubas-M	County: Stark;	10636 (3241.9)	middle Bakken member
Kubas-M/L	Operator: Whiting Oil & Gas Corp; Field: Bell	10638 (3242.5)	lower/middle Bakken member

All core fragments were subsampled into: (1) thin sections (150 μm thick) and granular size fractions (177-500 μm) for SANS and USANS measurements; (2) cuboids (1.0±0.05 cm length) for MICP analyses; (3) thin slabs for FE-SEM imaging; and (4) powders (<75 μm) for X-ray diffraction (XRD) and total organic carbon (TOC) content tests.

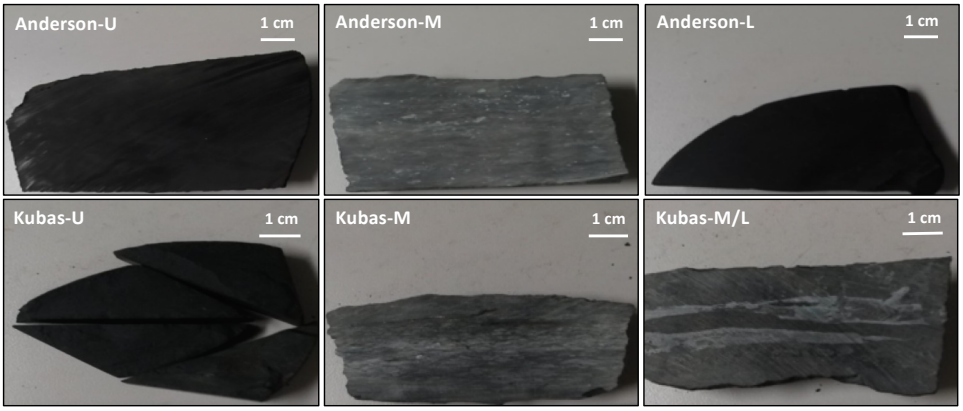

Figure 2. Optical images of core fragments from Anderson and Kubas wells.

The quantitative mineralogy was measured using Rigaku Ultima IV at the University of Oklahoma for Kubas samples and the operational procedures are illustrated in the work of Madden et al. (2006). The QXRD for Anderson samples were measured using the Shimadzu MAXima XRD-7000 X-Ray Diffractometer at the University of Texas at Arlington, which was operated using Cu Kα radiation with a scanning rotation from 2°-70° at room temperature, and each mineral was identified using the RDB-Minerals database with an averaged error of ~1%. The analysis of TOC contents was performed with Shimadzu solid sample module SSM-5000A and TOC-Vws Analyzer, by separately measuring total carbon (TC) (combustion at 900°C) and total inorganic carbon (TIC) (with 33% phosphoric acid to remove carbonates and combustion at 300°C) using a non-dispersive infrared detector. The TOC of each sample is obtained as the

difference between TC and TIC with an averaged error of ~10%. For FE-SEM imaging work, small off-cut block samples of about 1-cm square were polished to create a level surface using dry emery paper, milled by argon-ion, and mounted to SEM stubs using carbon paste to provide a conductive surface layer with Zeiss Merlin Compact at the Institute of Geology and Geophysics, Chinese Academy of Sciences. Images were collected at an acceleration voltage of 5 kV with a working distance of 4-6 mm.

2.2 (U)SANS Measurements

2.2.1 (U)SANS data collection and reduction

Neutrons are weakly interacting particles and, therefore, ideally suited for nondestructive probing of large (relative to other scattering methods) sample volumes. As opposed to fluid invasion methods such as helium expansion, MICP, and low-pressure gas physisorption, neutron scattering is capable of measuring the structure of both connected (accessible) and isolated (inaccessible) pores (e.g., Clarkson et al., 2013; Melnichenko, 2016; Zhao et al., 2017; Yang et al., 2017).

The basis of SANS and USANS experiments is relatively straightforward. A nearly monochromatic neutron beam is incident upon a sample and, upon interacting with atomic nuclei within the sample, neutrons are scattered at some angle, 2θ, with respect to the incident neutron flight direction. For SANS, a scattering pattern is recorded from a two-dimensional area detector positioned some distances from the sample (Melnichenko, 2016). USANS, which uses the Bonse-Hardt-technique to extend to smaller scattering angles, measures horizontal structures orthogonal to the initial neutron flight direction, so it inherently yields 1-D information. The resulting scattering information smears vertically and is often processed using a desmearing algorithm to be directly compared with SANS results. The scattering data are typically reported

as the intensity of scattered neutrons at a given momentum transfer or scattering vector, $I(Q)$, where

$$Q = 4\pi\lambda^{-1}\sin\theta \quad (1)$$

λ is the neutron wavelength and 2θ is the scattering angle. Radliński et al. (2000) showed that, to a first approximation, the size of the scattering object r (pores in the case of porous materials such as rocks) is related to Q as $r \cong 2.5/Q$.

In disordered systems like rocks, neutrons scatter coherently from spatial variations in coherent neutron scattering length density (SLD), ρ. The intensity of scattered neutrons is proportional to the neutron contrast factor, defined as the square of the difference between the SLD of a scattering object and its surrounding medium (Melnichenko, 2016).

$$I(Q) \sim (\Delta\rho)^2 = (\rho_1 - \rho_2)^2 \quad (2)$$

The neutron SLD value of the most common crustal minerals lies in the range of (3-4)×10^{10} cm^{-2}. As such, a scattering contrast in rock samples arises primarily from the interface between the solid rock matrix constituent and the void spaces of the rock (SLD of air and vacuum is ~ 400 and 0 cm^{-2}, respectively). The solid matrix of shale is a complex array of numerous components, such as minerals and OM. The calculation of the average neutron SLD of such a multi-component matrix is commonly carried out as a volume average over all components, according to Equation 3

$$\langle\rho\rangle_{matrix} = \sum_{i=1}^{n} \phi_i \rho_i \quad (3)$$

where index i indicates a component, n is the total number of components, ϕ_i is the volume fraction of the i-th component, and ρ_i is the neutron SLD of the i-th component, which can be obtained using the online neutron scattering calculator provided by the NIST Center for Neutron Research (NCNR) at https://www.ncnr.nist.gov/resources/activation/. Table 2 lists the density,

Table 2. Formula, density, molecular weight, and computed neutron SLD for various components of the selected six Bakken shale samples.

Compound	Formula	Density (g/cm^3)	Molecular Weight (g/mol)	SLD_i (10^{10} cm^{-2})
Albite	$NaAlSi_3O_8$	2.62	263.02	3.96
Anorthite	$Ca(Al_2Si_2O_8)$	2.73	277.41	3.93
Calcite	$CaCO_3$	2.71	595.22	4.69
Clinochlore	$(Mg,Fe,Al)_6(Si,Al)_4O_{10}(OH)_8$	2.65	595.22	3.46
Dolomite	$MgCa(CO_3)_2$	2.84	184.40	5.40
Gypsum	$CaSO_4 \bullet 2(H_2O)$	2.32	172.17	2.26
Illite	$(K,H_3O)(Al,Mg,Fe)_2(Si,Al)_4O_{10}[(OH)_2,(H_2O)]$	2.75	389.34	3.49
Kaolinite	$Al_2Si_2O_5(OH)_4$	2.60	258.16	3.18
Orthoclase	$KAlSi_3O_8$	2.56	278.33	3.66
Marcasite	FeS_2	4.89	119.98	3.72
Muscovite	$KAl_2(AlSi_3O_{10})(F,OH)_2$	2.82	398.71	3.93
Plagioclase	$(Na,Ca)(Si,Al)_4O_8$	2.68	270.77	3.96
Pyrite	FeS_2	5.01	119.98	3.81
Quartz	SiO_2	2.65	60.085	4.18
Organic matter	*Variable*	1.22	*Variable*	2.0 - 3.5

molecular weight, and computed neutron SLD_i for components of the studied samples as identified from quantitative XRD and TOC analysis. The volume fraction of an individual component is calculated based on its mass percentage and grain density. The thermal maturity, and thereby the chemical composition, of OM (kerogen or bitumen), varies with burial history. As such, the SLD of TOC is likewise variable. Following the work of Thomas et al. (2014), we set the minimum and maximum values of SLD for TOC as 2.0×10^{10} cm^{-2} and 3.5×10^{10} cm^{-2}, corresponding to vitrinite reflectance values of 0.8-1.5 (% R_o) likely encountered for Bakken shale (Chen et al., 2009; Kuhn et al., 2012; Liu et al., 2017).

The scattering from randomly oriented granular materials allows for the collection of structural information averaged over all sample orientations (Bahadur et al., 2014; Melnichenko, 2016). Two types of sample forms, granular and thin section, are used in this (U)SANS work. Anderson samples used for (U)SANS tests were disaggregated with a mortar and pestle, and then wet sieved to achieve a particle diameter of 177-500 μm, which is thin enough to reduce multiple scattering to tolerable levels (Melnichenko, 2016). Sample particles were then oven-dried at 60°C prior to loading into pre-assembled titanium sample cells between two quartz glass windows spaced 1.0 mm apart, yielding an estimated effective neutron path length of ~0.5 mm.

Kubas samples for (U)SANS analyses were cut along the shale's bedding orientation such that the beam is oriented perpendicular to the bedding plane during scattering. This ensures a symmetrical 2-D scattering pattern on the detector, which can then be radially averaged to yield a 1-D scattering curve. Sample fragments were mounted on quartz slides optimized for neutron scattering and machined to 150 μm in thickness, to prevent significant multiple scattering (Vineyard, 1954; Gu et al., 2015). During scattering tests, the thin sections were mounted to cadmium plates with 3/8" (~9.5 mm) circular apertures.

SANS experiments were performed on the NG7 30m SANS instrument at NCNR (Glinka et al., 1998). A wide Q range was obtained by collecting SANS data at four sample-to-detector geometries of 1 m, 4 m, 13 m, and 13 m with a neutron focusing lens. A constant-frequency, rotating velocity selector constrained the incident neutrons to a fixed wavelength (λ) of 6.0 Å (1 m, 4 m, 13 m) and 8.09 Å (13 m w/lens), respectively ($\Delta\lambda/\lambda = 14\%$). The resulting raw, 2D scattering patterns (Figure 3a) were corrected for background and empty-cell scattering, detector efficiency, as well as irradiated sample volume and neutron transmission. Corrected scattering patterns from each detector geometry were then normalized relative to the open neutron beam intensity, radially averaged, and combined to yield a single, absolute scale, 1-D scattering profile (Figure 3b) covering a Q-range of 10^{-3} Å^{-1} $\leq Q \leq$ ~0.5 Å^{-1} (Kline, 2006).

USANS experiments were performed with the BT5 perfect crystal diffractometer USANS instrument at the NCNR using a neutron wavelength of 2.4 Å ($\Delta\lambda/\lambda = 6\%$) and Q-range of 2.5×10^{-5} Å^{-1} $\leq Q \leq 10^{-3}$ Å^{-1}. We employed Lake's algorithm (Lake, 1967) to desmear USANS data, which allowed for the graphical interpretation of USANS and SANS curves on the same plot of an absolute scale (Kline, 2006). The desmeared USANS data and SANS data were then combined into a final 1-D scattering curve covering a Q-range from 2.5×10^{-5} Å^{-1} to ~0.5 Å^{-1} (Figure 3c). Assuming that the dominant contribution to scattering at a given Q-value is from a pore with a radius $r \cong 2.5/Q$, this Q-range corresponds to a pore radius range of ~0.5 nm to 10 μm. However, in the following data analysis, the practical limits of this range are constrained due to experimental and data reduction limitations which will be discussed in Section 3.3.2.

The background scattering intensity, mostly caused by incoherent scattering of hydrogen atoms in OM or coherent scattering that arises from very small pores in the rock matrix (Bahadur et al., 2015; Melnichenko, 2016), of each sample was obtained from the slope of a plot of $Q^4I(Q)$

vs. Q^4 (Figure 3d) (Anovitz and Cole, 2015). The background-subtracted profile is then obtained after subtracting the background intensity value from each data point in the scattering curve (Figure 3e).

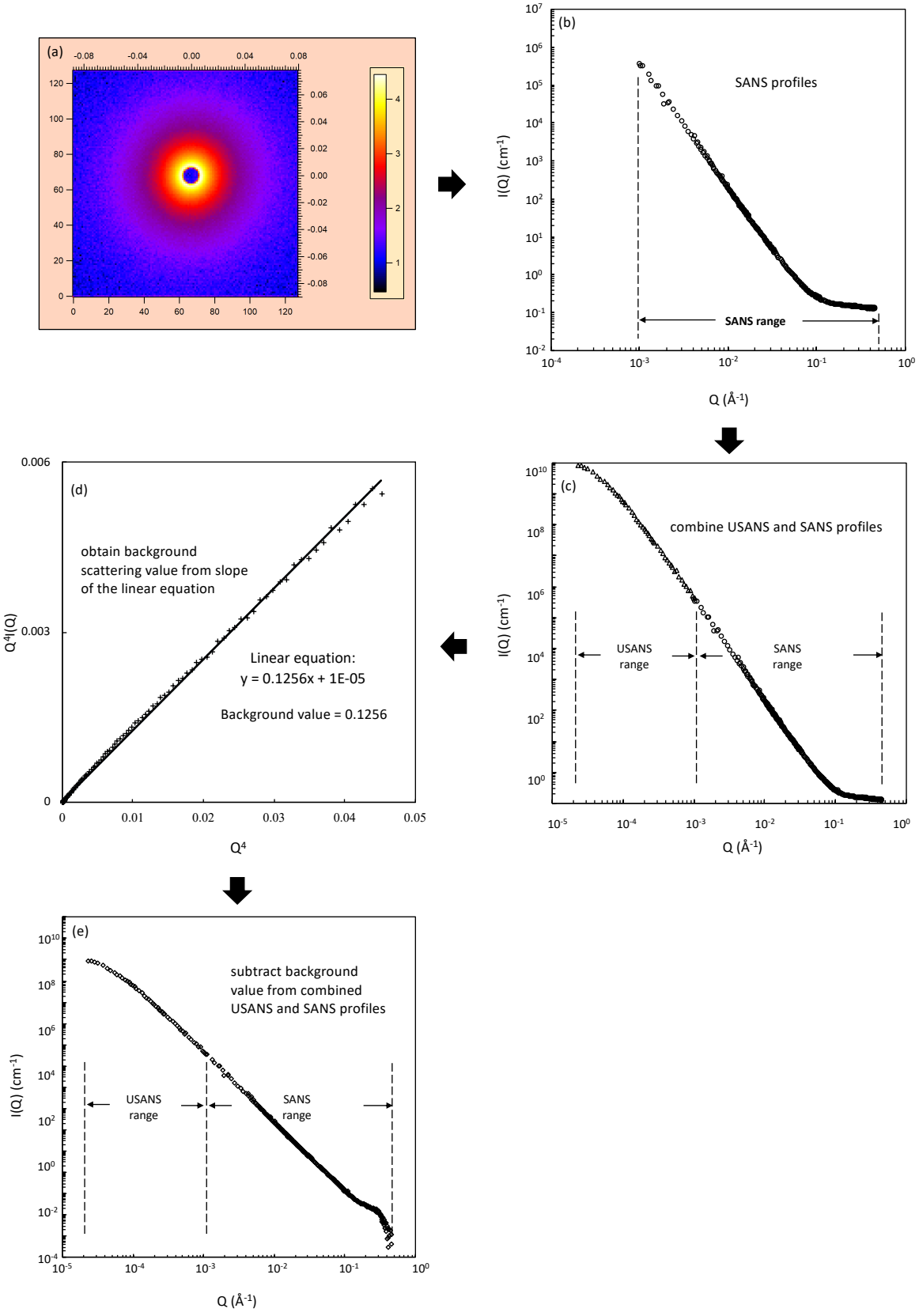
(a)
(b)
SANS profiles
I(Q) (cm-1)
Q (Å-1)
SANS range
(c)
combine USANS and SANS profiles
USANS range
SANS range
(d)
obtain background scattering value from slope of the linear equation
Linear equation: y = 0.1256x + 1E-05
Background value = 0.1256
Q4I(Q)
Q4
(e)
subtract background value from combined USANS and SANS profiles

Figure 3. Workflow of (U)SANS data processing: (a) Example of raw 2D scattering pattern collected by SANS neutron detector at 4_m. (b) Averaged 2D data from the four sample-detector geometries with 1 m, 4_m, 13_m, and 13_m lens. (c) Combined SANS and desmeared USANS scattering to yield full scattering profiles. (d) Background scattering estimate and linear equation. (e) A combined USANS and SANS profile with the background removed.

2.2.2 Scattering data analyses: Polydisperse spherical pore (PDSP) model and Porod invariant

To derive pore size distribution from neutron scattering data, pore systems in sedimentary rocks with fractal surfaces are usually idealized as polydisperse ensembles of spherical pores that span a broad size distribution in the sample (Schmidt, 1982; Melnichenko, 2016). In this work, we employ a polydisperse spherical pore (PDSP) model to describe the micro- and nano-pore architecture of the Bakken shales.

For a simple monodisperse system of spheres, the absolute scattering intensity can be mathematically expressed as the following equation (Hinde, 2004):

$$\frac{d\Sigma}{d\Omega} \equiv I(Q) = (\rho_1 - \rho_2)^2 \phi_p (1 - \phi_p) V_r F_{sph}(Qr) \tag{4}$$

where $V_r = (4/3)\pi r^3$ is the volume for a sphere with radius *r*; ϕ_p is the volume fraction of spheres in the scattering system; ρ_1 and ρ_2 are the SLD_S of surrounding medium and spheres, respectively; and $F_{sph}(Qr)$ is the form factor of a sphere with radius *r*:

$$F_{sph}(Q_r) = \left[3\frac{sin(Qr) - Qrcos(Qr)}{(Qr)^3}\right]^2 \tag{5}$$

To incorporate polydispersity into the model, Eq. 4 is adapted with a size distribution factor, $f(r)$ (Radlinski, 2004) to yield:

$$I(Q) = \frac{d\Sigma}{d\Omega}(Q) = (\rho_1 - \rho_2)^2 \frac{\phi_p}{\bar{V}_r} \int_{R_{min}}^{R_{max}} {V_r}^2 f(r) F_{sph}(Qr)\, dr \quad (6)$$

in which $\bar{V}_r = \int_0^\infty V_r\, f(r) dr$ represents the averaged pore volume; $f(r)$ is the power-law pore size distribution factor, which can be expressed as

$$f(r) = \frac{r^{-(1+f_D)}}{(r_{min}^{-f_D} - r_{max}^{-f_D})/f_D} \quad (7)$$

and r_{min} and r_{max} are the minimum and maximum pore radii (Hinde, 2004). However, it is noteworthy that this PDSP model is idealized by simplifying other pore shapes (e.g., cylinder, slit, and ink-bottle, as well as micro-fractures) in the rock system into equivalent spheres. Background-subtracted scattering profiles are loaded into the PRINSAS software (Hinde, 2004) and only fitted to the power-law scaled data, to generate the porosity and pore size distribution.

In addition to PDSP modeling, model/assumption-free Porod invariant analysis is applied for an evaluation of total porosity (Porod, 1952; Radlinski, 2006), using the following equation:

$$Y \equiv \int_0^\infty Q^2 I(Q)\, dq = 2\pi^2 (\Delta\rho)^2 \phi_p \left(1 - \phi_p\right) \quad (8)$$

where Y is the Porod invariant, ϕ_p is the pore fraction in the two-phase (matrix-pore) system. The combined (U)SANS data were analyzed using the Porod invariant approach by the SASVIEW software (http://www.sasview.org/). In the actual data processing, the integration in Eq. 8 has upper and lower limits which are determined by the maximum and minimum Q-value of each sample's scattering profile. Therefore, our porosity results are based on detectable size ranges of 1.25-500 nm (SANS) and 500 nm-20 μm (USANS).

2.3 Mercury injection capillary pressure analysis

While neutrons scatter from accessible and inaccessible porosity indiscriminately, fluid invasion methods such as MICP only measure pore systems connected to the boundaries of a sample and, therefore, provide complementary information about the total volume and size distribution of edge-accessible (i.e., connected to the sample surface) porosity.

MICP tests in this study were performed using a mercury porosimeter (Micromeritics AutoPore IV 9510) to characterize the pore structure from μm- to nm-scales. Prior to MICP tests, cuboid samples were oven-dried at ~60°C for at least 48 hours to remove the moisture and then cooled down to room temperature (~23°C) in a desiccator (Gao and Hu, 2013). During the test, a single cuboid was emplaced into a penetrometer suitable for low-porosity (~5%) samples such as shale, evacuated, enclosed by mercury, and then subjected to increasingly applied pressures. An initial filling pressure of 5 psi (0.034 MPa) ensured that the mercury fully enclosed the cuboid sample surfaces and minimized the conformance effect (e.g., Hu et al., 2017; Davudov and Moghanloo, 2018). Incrementally increasing the pressure to a maximum value of 60,000 psi (413 MPa) forced the non-wetting mercury to invade into the sample and occupy the volume of all the edge-accessible pores. To observe the size effect on edge-accessible porosity, in addition to cuboid shale samples, we performed MICP measurement on the same group of Bakken samples with two different grain sizes (500-840 μm and 177-500 μm) to obtain both inter- and intra-granular porosities, by using a low filling pressure of 0.2 psi to separate inter-granular pore spaces from intra-granular ones with the increasing pressures; this is validated with the quartz sands with similar grain sizes.

MICP measures bulk density, skeletal density, edge-accessible porosity, and pore-throat size distribution (Webb, 2001; Gao and Hu, 2015). The pore-throat diameter D (cm) is determined by the Washburn Equation (Washburn, 1921):

$$D = -\frac{4\gamma \cos \theta_c}{P} \tag{9}$$

with γ is the surface tension (485 dyne cm^{-1}), θ_c is the contact angle (130º), and P is the applied pressure (dyne cm^{-2}). The corresponding pore-throat diameter ranges from 3 nm (at the highest achievable pressure of 413 MPa) to 36 μm (at the filling pressure of 0.034 MPa). Wang et al. (2016) proposed that the contact angle of mercury in a circular pore increases exponentially as pore size decreases, an effect that becomes pronounced in nano-pores. Therefore, a corrected Washburn equation reported by Wang et al. (2016), with variable contact angle and surface tension as a function of pore size, was adopted for shale samples to derive a pore-throat size distribution ranging from 2.8 nm to 50 μm (Hu et al., 2017).

3. Results and Discussion

3.1 Mineralogical composition and TOC content

The XRD data, as well as the TOC contents of six Bakken samples, are given in weight percentage in Table 3. The three black shales, i.e., Anderson-U, Kubas-U, and Anderson-L, have very high TOC contents (up to 21.6 wt.%), which is consistent with most reported work of lower/upper Bakken members (Smith and Bustin, 1998; 2000; Jin and Sonnenberg, 2012; Borcovsky et al., 2017); these samples also have a similar pyrite content of around 6.0 wt.% which are formed in the early-middle diagenetic events (Kowalski and Sonnenberg, 2011). On the other hand, in three calcareous siltstones, Anderson-M and Kubas-M have a high proportion

Table 3. Averaged weight percentage and normalized volume percentage (in parenthesis) of mineralogical compositions and organic matters with calculated maximum and minimum SLDs ($\times 10^{10} cm^{-2}$) of six samples.

Component ID	Composition wt.% (vol.%)					
	Anderson-U	Anderson-M	Anderson-L	Kubas-U	Kubas-M	Kubas-M/L
Albite	-	-	-	-	2.7 (2.6)	0.5 (0.5)
Anorthite	-	-	-	3.1 (2.4)	-	-
Calcite	-	21.2 (23.2)	-	2.2 (2.1)	45.4 (48.3)	1.1 (1.4)
Clinochlore	-	-	-	7.1 (5.4)	-	0.2 (0.2)
Dolomite	9.0 (5.6)	8.0 (6.5)	8.5 (4.5)	6.8 (4.8)	6.8 (5.4)	59.6 (53.4)
Gypsum	-	-	-	3.1 (2.6)	-	-
Illite	3.4 (2.5)	1.0 (0.9)	16.7 (10.2)	-	-	-
Kaolinite	-	-	0.2 (0.1)	-	-	-
Marcasite	-	-	-	3.6 (2.5)	-	-
Muscovite	21.9 (16.0)	12.8 (12.2)	33.7 (20.8)	7.1 (5.8)	13.1 (12.1)	11.2 (11.8)
Orthoclase	18.1 (14.0)	5.3 (5.3)	7.7 (5.0)	26.0 (21.4)	7.8 (7.2)	10.4 (10.9)
Plagioclase	-	2.2 (2.1)	-	-	-	-
Pyrite	5.8 (4.3)	1.5 (1.5)	5.5 (3.5)	6.7 (5.7)	1.2 (1.1)	2.1 (2.3)

Quartz	41.8 (31.7)	47.9 (47.2)	28.4 (18.1)	34.3 (29.3)	23.0 (22.0)	14.9 (16.3)
TOC	13.7 (25.8)	0.5 (1.1)	21.6 (37.8)	9.8 (18.0)	0.6 (1.4)	1.4 (3.3)
Minimum SLD	3.54	4.28	3.25	3.60	4.38	4.67
Maximum SLD	3.93	4.30	3.82	3.87	4.40	4.72

Hyphen (-) indicates component not detected. Mass percentage of minerals and TOC is separate, but normalized volume percentage of all components include TOC.

of calcites (21.2 and 45.4 wt.%) and relatively low proportion of dolomites (8.0 and 8.5 wt.%) which are possibly authigenic carbonate cements (Pitman et al., 2001); Kubas-M/L has a very high percentage of dolomite (59.6 wt.%) which could be related to dolomitization (Sonnenberg and Pramudito, 2009; Kowalski and Sonnenberg, 2011). Compared with organic-rich shales, all three calcareous siltstones have a low TOC value (0.5 - 1.4 wt.%). Furthermore, all six samples have a modest percentage (<25 wt.%) of clay minerals except Anderson-L which has an over 50 wt.% of clay content.

3.2 FE-SEM images for pore types

Limited by the amount of Kubas samples, only three Anderson samples were subjected to FE-SEM imaging (Figure 4). Different pore types, such as intraparticle, interparticle, and organic pores, are observed in these samples. Interparticle pores, e.g., pores between grains, micro-cracks developed between minerals and organic matters, or clay-related pores, are widely distributed in the rock matrix. Intraparticle pores like intercrystalline pores in pyrite framboids or cleavage pores in mica are also easy to identify as there is a high proportion of pyrites and muscovites in the samples. OM pores are developed in the organic matters (either kerogen or bitumen) of the lower/upper black shales. Unlike Barnett Shale which has massive large OM pores, few large organic pores (>500 nm) are observed in the Bakken samples, which is consistent with the findings of Liu et al. (2017). Based on the classification of OM pores (Ko et al., 2017), we identified several primary OM pores (>1 μm), a few large bubble pores (200 nm - 1 μm), and to a much larger extent small spongy pores (<200 nm) which are randomly distributed in the organic matters (Figures 4a, c). Though these nano-scaled organic pores are fairly small, considering the large quantity of organic matter in the upper and lower Bakken shales, they could

contribute a significant amount to the total porosity. In contrast, the middle Bakken calcareous siltstone are primarily dominated by a large amount of inter-particle and intra-particle mesopores (2-50 nm) and macropores (>50 nm) which are generally larger than those in lower/upper Bakken (Figure 4b).

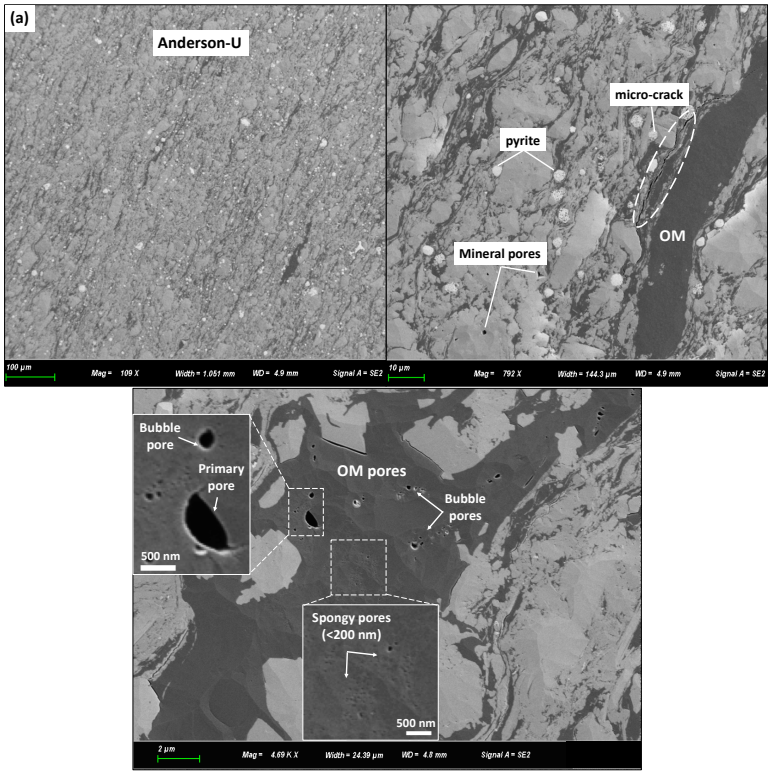

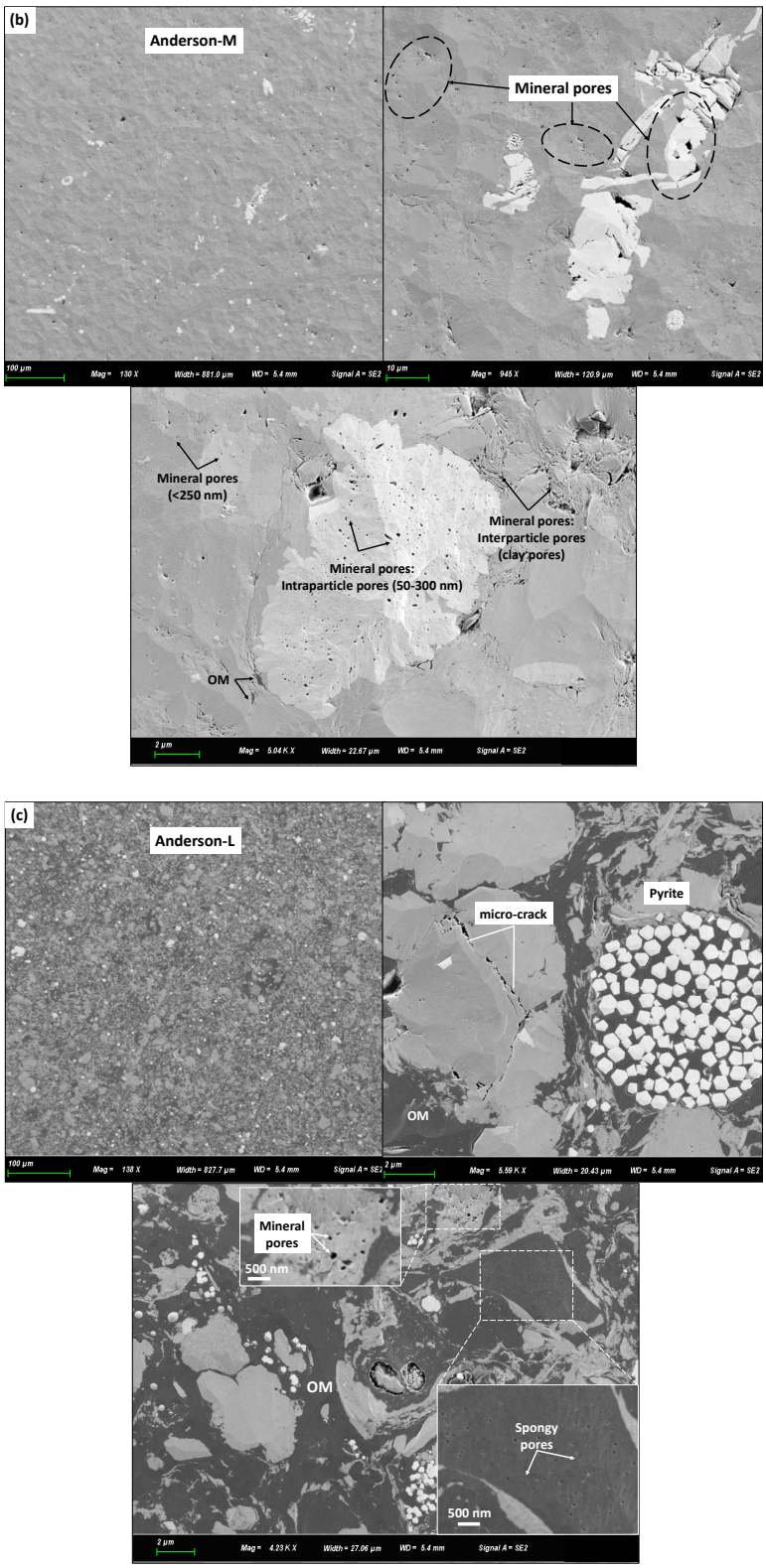

Figure 4. FE-SEM images of (a) upper Bakken shale with large bubble and spongy pores developed in organic matter (OM); (b) middle Bakken shale with a large amount of nano-scale mineral pores; (c) lower

Bakken shale with spongy pores concentrated on part of the OM. Organic matter: dark grey; pores: black; quartz, feldspar, carbonates, and clays: light grey; pyrite: white.

3.3 (U)SANS measurements

3.3.1 Characteristics of (U)SANS scattering intensities

Table 3 lists the normalized volume fraction (including TOC), ϕ_i, and computed minimum and maximum $\langle\rho\rangle_{\text{matrix}}$ of each shale sample, showing the SLDs range between ~3-5 (10^{10} cm^{-2}). The minimum and maximum value of $\langle\text{SLD}\rangle_{\text{matrix}}$ varies in the range of 3×10^{10} cm^{-2} to 4×10^{10} cm^{-2} for three organic-rich shales; while for the other three carbonate-rich samples, the maximum and minimum values of $\langle\text{SLD}\rangle_{\text{matrix}}$ are quite close in the range of 4×10^{10} cm^{-2} to 5×10^{10} cm^{-2}.

Previous observations indicate that an incoherent background scattering is primarily a function of hydrogen content in rocks such as shale (Ruppert et al., 2013; Anovitz and Cole, 2015). Our results are consistent with this observation, as samples with higher TOC exhibit higher incoherent background scattering intensities. The combined USANS and SANS data, before and after background subtraction, are shown in the log-log plots of Figure 5.

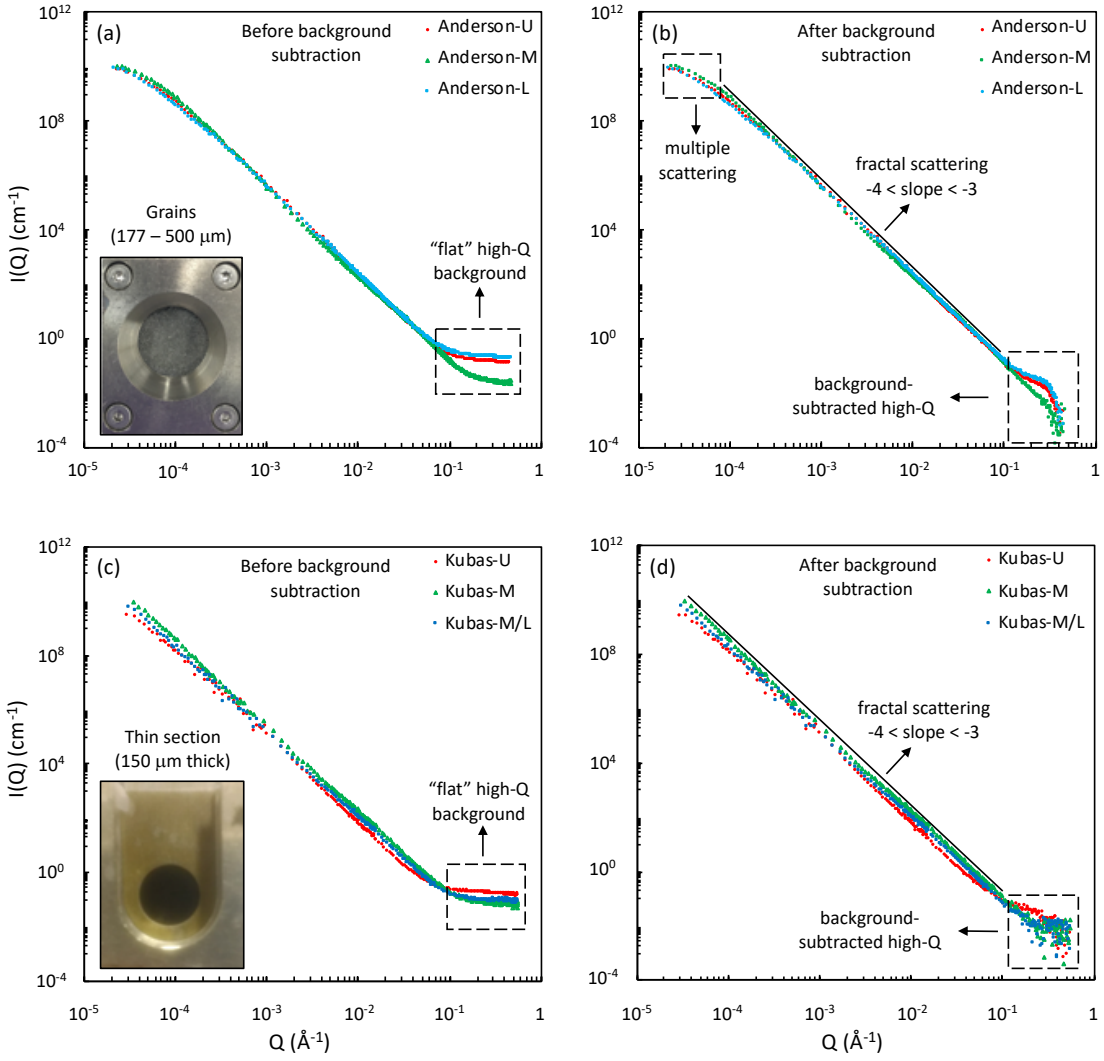

Figure 5. Combined (U)SANS scattering profiles for Anderson samples before (a) and after (b) background subtraction; Kubas samples before (c) and after (d) background subtraction.

In Figure 5a, the scattering profiles for Anderson samples exhibit the following qualitative characteristics: (1) scattering curves are overlapped in the mid-Q range (10^{-4} – ~0.1 Å^{-1}) with a linear relationship (i.e., an identical slope); (2) there is a slight rollover at low-Q range (2.5×10^{-5} - 10^{-4} Å^{-1}), which is attributable to multiple scattering (Melnichenko, 2016). The scattering

intensities of Kubas samples (Figure 5c) show similar scattering patterns with Anderson samples, but with some discrepancies: (1) no apparent break in the slope at low-Q; (2) the slope varies between samples at intermediate Q-values.

Figures 6b and 6d depict background-subtracted scattering intensity as a function of Q. High-Q scattering feature, arising from pores of 1.25-5 nm in diameter, is exhibited in most of the samples, especially for three lower/upper Bakken shales.

3.3.2 Porosity and pore size distribution from (U)SANS analyses

The PDSP model and Porod-invariant analysis were employed to process the SANS data (Q = 0.001 - 0.4 $Å^{-1}$) and combined SANS/USANS data (Q = 2.5×10^{-5} - 0.4 $Å^{-1}$), respectively, to generate porosity and pore size distribution. The corresponding measurable pore size range is 1.25-500 nm for SANS, and 1.25 nm-20 μm for combined (U)SANS data, using $r \cong 2.5/Q$.

The meso- and macro-scopic structure of sedimentary rocks are normally characterized by fractal geometry, and the fractal part is statistically described by a power law which is governed by the growth of minerals and cements in the pore space (Katz and Thompson, 1985; Krohn, 1988; Thompson, 1991). Previous studies demonstrated that source rocks have fractal surfaces over three decades of the length scale, from 6 nm to about 4 μm (Radlinski et al., 1999). In the log-log plot of *I(Q)* vs. Q, the linear portion of the scattering curve represents the fractal geometry characteristic. Bahadur et al. (2014; 2016) proposed that scattering at high-Q range might come from both fractal pores and non-fractal pores, and thus we present the zoomed view of scattering profiles (background-subtracted) with fractal and non-fractal segments in the Q range of 0.01-1 $Å^{-1}$ for all six samples (Figure 6). The linear dashed lines are the extension of the power-law fitted segment of scattering curve in the low-middle Q range (< 0.1 $Å^{-1}$). A higher

scattering curve than the extended curve, which is like a "concave" at high-*Q*, indicates the scattering not only comes from fractal but also non-fractal pores (e.g., Figure 6a).

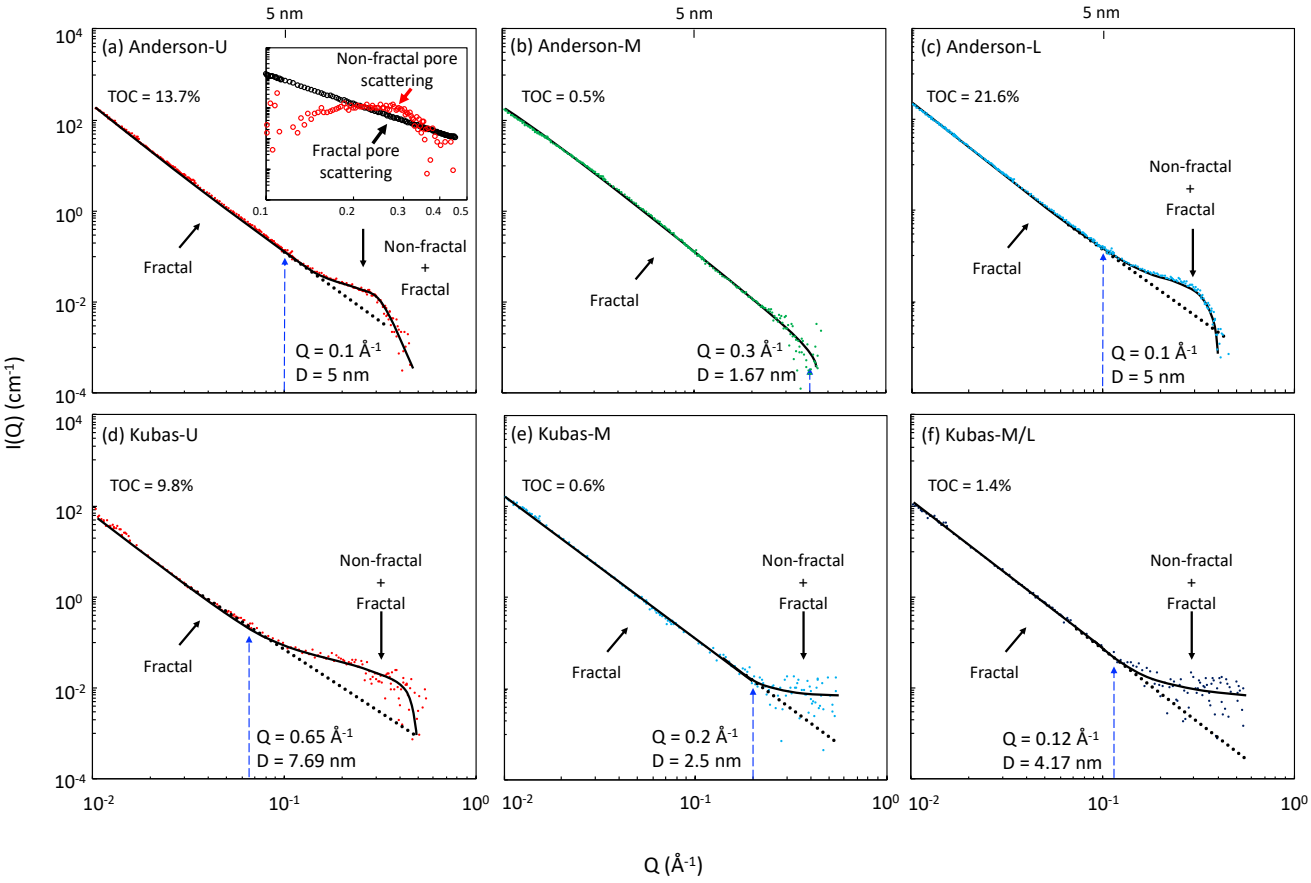

Figure 6. Mid- to high-Q regime of scattering profiles for six Bakken samples. The black curve depicts the shape of scattering profile, and the vertical blue dashed arrow indicates where a higher contrast occurs at high-Q. The scattering intensity at high-Q composes of fractal and non-fractal parts, and the black dots are extended data from the power-law fitted segments which represent scattering intensity contributed from fractal pores in this size range.

However, it should be noted that it is possible there are many non-fractal pores larger than 5 nm while their scattering intensities are relatively small compared with those from fractal pores, and therefore the overall scattering curves still exhibit a linear relationship in the low-middle Q range. Three organic-rich shales with TOC values exhibited very similar scattering curve shapes at high-Q (as shown in Figures 7a, c, d). The scattering curves start to deviate significantly from the power-law segment before or at Q=0.1 Å^{-1}, indicating a stronger scattering from non-fractal pores characterized by Euclidean geometry (Bahadur et al., 2014) smaller than 5 nm (most likely to be organic pores and/or clay platelet-related pores). However, for sample Anderson-M (Figure 6b) which has a very low TOC content (0.5 wt.%) but similar clay content (14 wt.%) with Kubas-U (16 wt.%), this high-Q "concave" feature is not observed, and thus the effect of clay-related pores is excluded here. In Anderson-M, the linear power-law distribution of the scattering data can go to Q=0.4 Å^{-1}, corresponding to a minimum pore diameter of 1.25 nm, showing a dominant presence of fractal pores in the entire pore system. As shown in Figures 7e-f, however, Kubas-M and Kubas-M/L exhibit another shape of scattering curve, in which the data points are more randomly scattered at high-Q, probably due to the effect of background noises during the SANS measurement.

Since PDSP model only applies to the fractal portion (power-law regime) of the scattering profile, it does not work for the shale with a "concave" at high-Q region. Some previous work discarded part of the scattering data at high-Q (> 0.1 Å^{-1}) in order to fit the linear portion on the log-log scale (Radlinski et al., 2004), and thus lose the information from pores smaller than 5 nm. In our analysis, we extend the straight line (black data points in Figure 6a) from where it ends (e.g., Q = 0.1 Å^{-1} for Anderson-U) to the maximum Q value based on the power-law relationship, and then subtracted it from the total scattering intensity to obtain the non-fractal

pore scattering intensity (red data points in Figure 6a). By extending the fractal portion to Q = 0.3 Å^{-1} for all six samples, we then fit them to the PDSP model using the PRINSAS and derive sample's porosity (Table 4) as well as pore size distribution (Figure 7).

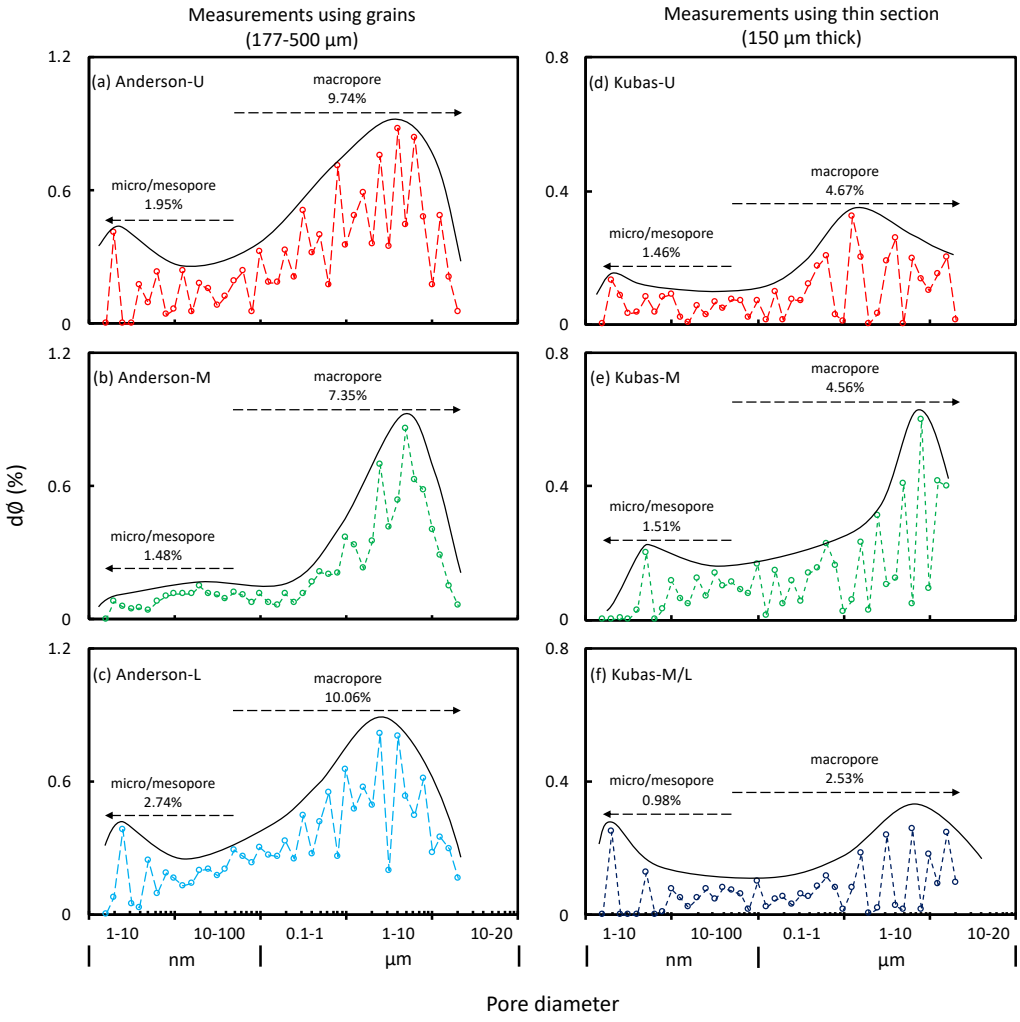

Figure 7. (U)SANS-generated pore size distribution (using PDSP model) shows the porosity change in the detectable pore size range from 1.25 nm to 20 µm for six Bakken samples; the dashed line represents a porosity change based on the data points, and the black solid curve shows a general trend of porosity change. The dashed arrows show the total porosity of micropores and mesopores (in the range from 1.25 nm to 50 nm) as well as the total porosity of macropores (in the range from 50 nm to 20 µm).

Table 4. Porosity values (%) obtained from (U)SANS (sample size: 177-500 μm grains) and MICP (sample size: 1-cm cubes) analyses

Sample ID	MICP	SANS (PDSP)	SANS (Porod)	SANS+USANS (PDSP)	SANS+USANS (Porod)
Anderson-U	2.29 (8.54[1]; 13.23[2])	6.18 ± 0.65	5.42 ± 0.60	11.69 ± 1.22	13.10 ± 1.60
Anderson-M	3.71	3.46 ± 0.02	3.05 ± 0.02	8.83 ± 0.04	9.82 ± 0.05
Anderson-L	2.91	7.53 ± 1.21	6.94 ± 1.20	12.80 ± 2.05	14.75 ± 2.85
Kubas-U	1.62	4.66 ± 0.34	3.31 ± 0.25	6.13 ± 0.45	5.19 ± 0.40
Kubas-M	2.76	3.26 ± 0.02	2.91 ± 0.01	6.07 ± 0.03	5.88 ± 0.03
Kubas-M/L	0.98	2.13 ± 0.02	1.77 ± 0.02	3.51 ± 0.04	3.23 ± 0.04

Color bars (for relative comparison) represent a fixed scale of 0-15% porosity. Measurable range: MICP: 2.8nm < $D_{pore\ throat}$ < 50 μm; SANS: ~1 nm < D_{pore} < 500 nm; SANS+USANS: ~1 nm < D_{pore} < 20 μm. The porosity is expressed as the average value plus/minus errors.

[1]measured MICP porosity using grain size of 500-840 μm; [2]measured MICP using grain size of 177-500 μm.

To obtain Porod-invariant porosity, the raw scattering data of all samples were loaded into the SASVIEW with SLDs and background values entered in the program. Unlike the PDSP model, the Porod invariant analysis is expected to yield the volume of all pore spaces in the measurable size range regardless of the pore shapes, and results are also listed in Table 4.

3.4 Pore structure characteristics from MICP analyses

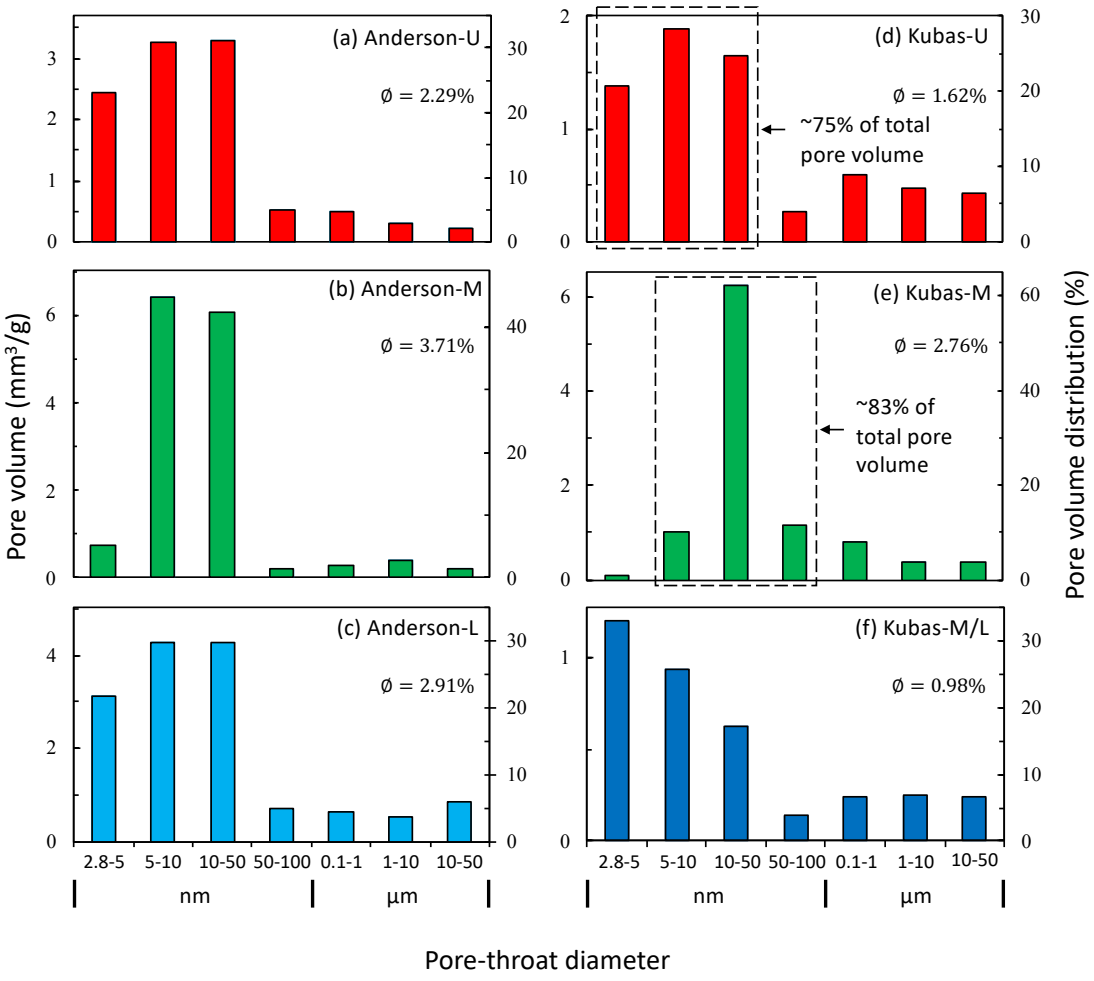

Figure 8. MICP-generated pore volume/pore volume distribution versus pore-throat size histograms for six Bakken samples from nanometer to micrometer scale (pore-throat size range: 2.8 nm to 50 □m). MICP measured porosity is given for each sample. The dashed box in (d) and (e) gives an example of comparison of total accessible pore volume between upper Bakken member organic-rich shale and middle Bakken calcareous siltstone.

Table 5. Pore structure characteristics of bulk density, skeletal density (in parentheses), porosity, total pore area, totoal pore volume, and pore body/throat ratio obtained from MICP analyses

Sample ID	Bulk density (Skeletal density) (g/cm^3)	Porosity (%)	Total pore area (m^2/g)	Total pore volume (mm^3/g)	Pore body/throat ratio for the pore-throat range of		
					2.8 - 5 nm	5 -10 nm	10 - 50 nm
Anderson-U	2.17 (2.22)	2.29	6.04	10.6	1.1 - 1.6	1.6 - 2.6	2.6 - 45
Anderson-M	2.58 (2.68)	3.71	7.11	14.4	4 - 5	5 - 100	>100
Anderson-L	2.02 (2.08)	2.91	7.86	14.4	1 - 1.5	1.5 - 2	2 - 18
Kubas-U	2.44 (2.48)	1.62	3.41	6.6	1.4 - 2.6	2.6 - 8	8 - 35
Kubas-M	2.65 (2.68)	2.82	2.29	10.1	9 - 10	10 - 50	>100
Kubas-M/L	2.70 (2.72)	0.98	2.12	3.6	2.3 - 4.6	4.6 - 15	15 - 50

Pore structure characteristics derived from MICP analyses are given in Table 5, and pore-throat size distribution vs. incremental pore volume of each sample is plotted to show the volume contribution in seven size intervals (Figure 8). The methodology adopted to obtain pore-throat size distribution are detailed in the literature (Gao and Hu, 2013; Hu et al. 2017).

In general, the bulk/skeletal densities of organic-rich shales in the lower/upper Bakken members are lower than carbonate-rich samples in the middle member (Table 5). The two middle Bakken samples have larger measured porosities (3.71% and 2.76%) than the lower/upper Bakken samples. The following distinct differences in pore-throat size distributions can be observed between three organic-rich shales and three calcareous samples:

(1) Anderson-U, Anderson-L, and Kubas-U (Figures 8a, c, e) have a similar pattern of pore-throat size distribution: they all possess dominant meso-scale pore-throats at 2.8-50 nm,

and the corresponding pore volumes (i.e., both pore bodies and pore throats) account for ~ 70-80% of total pore volume in the detectable size range.

(2) Anderson-M and Kubas-M have pore-throat sizes concentrated in 5-50 nm range (Figures 8b, e) with very few pore-throats smaller than 5 nm. In contrast, Kubas-M/L (Figure 8f), however, exhibits a predominant pore-throat size distribution at 2.8-10 nm range. Possible reasons include (a) an extensive carbonate cementation; (b) a porosity change during dolomitization; and (c) pore spaces having already been invaded by migrated bitumen (Figure 8f).

With 60,000 psi (413 MPa) as the highest pressure to be reached by the instrument, the MICP analysis can only probe pore-throats larger than 2.8 nm (diameter). However, a plot of log differential intrusion vs. pressure (Figure 9a), of sample Anderson-U as an example, indicates an existence of smaller pore spaces (D < 2.8 nm), because spikes at high pressures show a trend (dashed arrow in Figure 9a) of going up in the <5 nm region, meaning more smaller spaces could have been filled up by mercury under higher pressures. As a comparison, a similar plot for sample Anderson-M (Figure 9b) exhibits a single big spike around pore-throat diameter of 10 nm, indicating that there is no appreciable presence of smaller pores (D<10 nm) in this carbonate-dominated sample. These differences of predominant pore-throat sizes are typical features for lower/upper shale member and middle dolomite member, and consistent for other four samples (not shown).

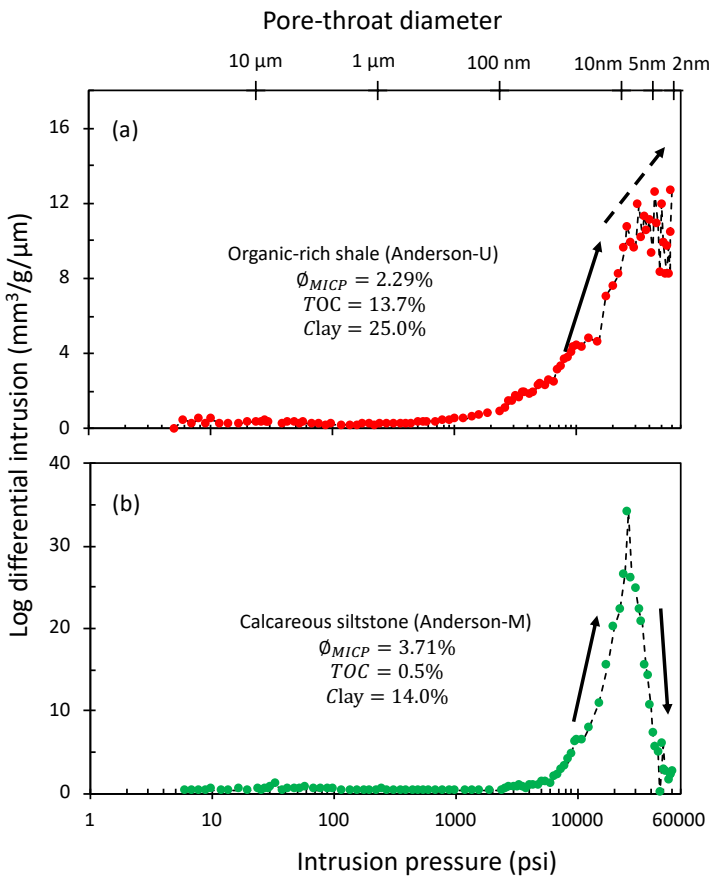

Figure 9. Mercury intrusion behavior for applied pressures from 5 psi (0.034 MPa) to 60,000 psi (413 MPa) showing characteristics of dominant connected pore networks in the (a) organic-rich black shale and (b) calcareous siltstone using samples from Anderson well as an example.

Pores with a throat diameter (D=2.8-10 nm) are probably related to organic matter-hosted pores or inter-clay platelet pores (Hu et al., 2017). In three organic-rich shales, the pore body/throat ratio, obtained from intrusion/extrusion branches of MICP tests (Hu et al., 2017), is around 1-3 when pore-throat diameter is smaller than 10 nm, indicating the spherical or elliptical pore shape of OM spongy pores. As a contrast, pore spaces at the pore-throat diameter of 10-50 nm are probably mainly related to inter-granular pores in fine-grained mudrocks, from our MICP work on shallow and "homogeneous" siltstone and claystone which is consistent with expected

pore sizes estimated for cubic (most loose) and rhomohedral (most tight) packing of uniform-sized grains (data not shown). While for carbonate-rich middle Bakken, the pore body/throat ratio is generally large, indicating a predominant presence of cylindrical pores which are mostly mineral pores as shown in SEM images (Figure 4b). In shales and mudstones, mineral grains can have a variety of shapes and sizes. As a general rule, clay minerals are lath-shaped and mainly <10 μm in diameter to deposit mainly as isotropic flocs or aggregates (e.g., Day-Stirrat et al., 2008). In contrast, minerals like quartz and feldspar are more equidimensional and mainly > 10 μm. There are exceptions to this rule, as clay minerals like mica, kaolinite and chlorite can have diameters >10 μm to be coarser-grained to deposit as single grains (Day-Stirrat et al., 2008), and conversely non-clay minerals can be <10 μm. Mechanical compaction, smectite illitization and kaolinite-chlorite conversion can lead to diagenetic reorientation of phyllosilicate minerals (Day-Stirrat et al., 2008) and associated pore-scale properties (Aplin et al., 2006).

3.5 Result comparisons of (U)SANS and MICP approaches

3.5.1 Porosity

For comparison, (U)SANS and MICP measured porosities are compiled in Table 4. The MICP porosities are close to literature results of the Bakken Shale, for example, an average value of 3.6% for upper and lower Bakken shales (Hall et al., 1986; Sweeney et al., 1992); 1-16% with an average value of 5% for the middle Bakken (Pitman et al., 2001). The porosities generated from the PDSP model and the model-independent Porod invariant analysis are quite close, indicating that (1) the assumption of spherical pore shape is adequate for quantifying the porosity; and (2) the non-fractal pores smaller than 5 nm do not contribute significantly to the total porosity in the measurable pore size range. In comparison with the MICP porosity in which

the calcareous siltstones (except Kubas-M/L) have a larger measured porosity than organic-rich shales, the (U)SANS porosity exhibits an opposite feature of a general lower porosity in the middle member. Two possible reasons for the disparity of relative porosity difference include (1) the larger-sized cube samples used in the MICP measurement has a stronger effect from low pore connectivity (a higher proportion of isolated pores) for fine-grained mudrocks such as lower/upper Bakken shales. Furthermore, this connectivity effect is probably less pronounced for middle Bakken sample as it has larger predominant pore-throat size of 10-50 nm. (2) volume proportion of closed pores, especially OM pores, is higher in the lower/upper Bakken than the middle Bakken. And this closed porosity is only detectable by the neutron scattering technique rather than the fluid intrusion methods.

The size-dependent porosity, affected by pore connectivity, is evident from MICP and (U)SANS tests with different sample sizes. In general, the measured MICP porosity is relatively low (~1 to 4%) when using a larger-sized cubic sample, even though it has a slightly larger upper detection range (i.e., pore-throat size of 50 μm) than (U)SANS, which has the measured porosity of 3-15% using either grains (177-500 μm) or 150 μm-thick thin sections in the test. To investigate the sample size effect on porosity measurement, we performed MICP analysis on sample Anderson-U using two grain sizes (i.e., 500-840 μm and 177-500 μm), which yields a porosity of 8.54% and 13.23%, respectively. This indicates an increasing measured porosity with a decreasing sample granular size; the difference lies in the proportion of isolated pores, only detectable by (U)SANS, associated with poor pore connectivity of shales (Hu et al., 2012; 2015; Davudov and Moghanloo, 2018). By comparing MICP and (U)SANS results for the same sample size of 177-500 μm, we have 13.2% (MICP) and 13.1±1.60% (SANS/USANS) which are remarkably close, indicating that almost 100% of pores remain accessible to sample edges at this

grain size, consistent with the finding of a well-connected surface zone of 400 μm in thickness for the Barnett Shale from tracer studies (Hu et al., 2015). The implication for us is that under the geological condition, the upper and lower Bakken members have a vast volume of closed pores in the rock matrix which may have hydrocarbon trapped inside, and this closed porosity is not counted in the porosity measured by some traditional petrophysical approaches in industry (e.g., helium expansion method on core plugs).

3.5.2 Pore (throat) size distribution

Pore (throat) size distribution generated from (U)SANS and MICP techniques provide a more complete picture of pore structure in shale for total porosity. By using the PDSP model, we see the porosity change from SANS/USANS-derived pore size distribution, which generally shows a bimodal shape with pores ranging in 1.25-10 nm and 1-20 μm (Figures 8a, c-f), except for sample Anderson-M (Figure 7b). In contrast, MICP results indicate that a large portion of pore volume is from those pores connected by nm-scale pore-throats (2.8-50 nm) (Figure 9). This exhibits a feature that whatever the lithology of these rocks, pore-throats in the pore system are primarily of <50 nm in scale, but they could connect both large μm-scale (>1 μm) pores and smaller nm-scale (<1 μm) pores. King et al. (2015) mentioned a similar idea related to MICP technique that intruded volume is not explicitly related to pore throat size, a small pore throat may be associated with a large or a small pore. Slatt and O'Brien (2011) also reported about 50% pores larger than 1 μm without using Ar-milled samples for SEM approach. While Ar-ion milling provides an opportunity for detecting pores down to about 5 nm, the sample preparation under-estimates μm-sized pores due to clay floccules collapse from ion milling (Slatt et al., 2013).

For illustration purposes, Figures 8d and 8e compare Kubas-U with Kubas-M, with the former an organic-rich shale of a lower measured porosity (1.62%) than the latter which is carbonate-rich (2.76%). It is shown that around 75% of the total accessible pore volume is concentrated in the pores with pore-throats ranging from 2.8 to 50 nm in Kubas-U, while about 83% of the total pore volume is centered around pores with a pore-throat of 10-50 nm in Kubas-M. The apparent difference is that Kubas-U has more pore volume contributed by pores with smaller pore-throats (2.8-10 nm), and some of them are considered to be OM-hosted spherical/elliptical nanopores according to the pore body/throat ratio (i.e., 1.4 - 8) in Table 5, as well as FE-SEM images. In comparison, pores in Kubas-M are primarily connected by pore-throats larger than 10 nm, considering the large pore body/throat ratio (i.e., > 100; Table 5), these pores are more likely to be mineral pores of μm-scale. This observation explains the bimodal pore size distribution feature, especially in the organic-rich shale of Bakken Formation (Figure 7). Across the measurable size range (~1.25 nm - 20 μm), pores larger than 100 nm (either mineral pores or organic pores) dominate the entire pore system, and in the lower/upper Bakken, OM-pores (mostly <10 nm) contribute greatly to the total porosity.

4. Conclusions

In summary, this study presents results of applying (U)SANS and MICP techniques to investigate the pore structure of samples from the Bakken Formation. Assisted with mineralogy and TOC analyses, as well as FE-SEM imaging, (U)SANS and MICP measurements are able to indicate that the studied six Bakken samples have a broad range of pore lengths across nm-μm spectrum (~1.25 nm - 50 μm). A distinct difference in effective/total porosity and pore/pore-

throat size distribution can be yielded between the studied shale samples through this methodology. The main findings are two-fold:

(1) The studied three black shale samples from the lower and upper Bakken members with an abundance of organic matters (TOC: 9.8-21.6 wt.%) exhibit a modest amount of measurable effective (surface-accessible) porosity from MICP test, but a large total porosity (includes isolated porosity) from (U)SANS measurements. (U)SANS results of pore size distribution indicates that the majority of pores are widely distributed in the pore length range of ~1.25 nm - 20 μm, and a considerable proportion of micropores and meso-pores might be contributed by OM-hosted pores. In the meanwhile, a MICP-generated pore-throat size distribution points out that these multi-sized (μm-nm scale) pores in the pore system are primarily interconnected by pore-throats with a size of 2.8-50 nm;

(2) The studied calcareous siltstones from the middle Bakken member are more carbonate-rich with a very low TOC content. A higher MICP-measured effective (surface-accessible) porosity than lower/upper shales indicating a better reservoir quality. (U)SANS generated pore size distribution shows that a great portion of pores are larger than 100 nm, and most pores are connected by pore-throats with a size of 5-50 nm based on MICP results. Furthermore, the pore structure could change significantly as a result of burial diagenesis (e.g., dolomization). The pore/pore-throat size distribution is more similar to that of the organic-rich shales.

Through the comparison, we are able to see the middle Bakken samples have a higher effective porosity while the lower/upper Bakken samples have a larger total porosity. This confirms the utility of using middle Bakken as the stimulation zone for tight oil production, considering its more favorable pore architecture such as a relatively predominant presence of larger pore-throats. Although the sample sizes of six is not sufficient enough to represent the

entire Bakken Formation, the methodology proposed in this article is promising to understand the pore structure of tight rocks.

5. Acknowledgement

This research is funded by National Natural Science Foundation of China (Nos. 41672251 and 41830431), Open Funds of State Key Laboratory of Oil and Gas Reservoir Geology and Exploitation at Chengdu University of Technology (No. PLC-201602), AAPG Foundation's Grants-in-Aid Program, and National Science Foundation Graduate Research Fellowship (Grant No. 1144240). We thank Joseph Ikechukuwu Anyanwu for acquiring core samples from North Dakota Geological Survey, and Andy Madden of the University of Oklahoma for XRD analyses. Access to SANS NGB30 and USANS BT5 was provided by the Center for High Resolution Neutron Scattering, a partnership between the National Institute of Standards and Technology and the National Science Foundation under Agreement No. DMR-1508249. This work benefited from the use of the SasView application, originally developed under NSF award DMR-0520547. SasView contains code developed with funding from the European Union's Horizon 2020 research and innovation programme under the SINE2020 project, grant agreement No 654000. Certain commercial equipment, instruments, or materials are identified in this paper to foster understanding. Such identification does not imply recommendation or endorsement by the National Institute of Standards and Technology, nor does it imply that the materials or equipment identified are necessarily the best available for the purpose.

6. References

Anovitz, L.M., Cole, D.R., 2015. Characterization and analysis of porosity and pore structures, in: Reviews in Mineralogy and Geochemistry. pp. 61-164. https://doi.org/10.2138/rmg.2015.80.04

Aplin, A.C., Matenaar, I.F., McCarty, D.K., van der Pluijm, B.A., 2006. Influence of mechanical compaction and clay mineral diagenesis on the microfabric and pore-scale properties of deep-water Gulf of Mexico mudstones. Clays Clay Miner. 54, 500–514. https://doi.org/10.1346/CCMN.2006.0540411

Bahadur, J., Melnichenko, Y.B., Mastalerz, M., Furmann, A., Clarkson, C.R., 2014. Hierarchical pore morphology of cretaceous shale: A small-angle neutron scattering and ultrasmall-angle neutron scattering study. Energy and Fuels 28, 6336-6344. https://doi.org/10.1021/ef501832k

Bahadur, J., Medina, C.R., He, L., Melnichenko, Y.B., Rupp, J.A., Blach, T.P., Mildner, D.F.R., 2016. Determination of closed porosity in rocks by small-angle neutron scattering. J. Appl. Crystallogr. 49, 2021-2030. https://doi.org/10.1107/S1600576716014904

Bahadur, J., Radlinski, A.P., Melnichenko, Y.B., Mastalerz, M., Schimmelmann, A., 2015. Small-angle and ultrasmall-angle neutron scattering (SANS/USANS) study of New Albany Shale: A treatise on microporosity. Energy and Fuels 29, 567-576. https://doi.org/10.1021/ef502211w

Barker, J.G., Glinka, C.J., Moyer, J.J., Kim, M.H., Drews, A.R., Agamalian, M., 2005. Design and performance of a thermal-neutron double-crystal diffractometer for USANS at NIST. J. Appl. Crystallogr. 38, 1004-1011. https://doi.org/10.1107/S0021889805032103

Borcovsky, D., Egenhoff, S., Fishman, N., Maletz, J., Boehlke, A., Lowers, H., 2017. Sedimentology, facies architecture, and sequence stratigraphy of a Mississippian black mudstone succession - The upper member of the Bakken Formation, North Dakota, United States, AAPG Bulletin. https://doi.org/10.1306/01111715183

Brown, S., Yucel, M., 2013. The Shale Gas and Tight Oil Boom; https://www.cfr.org/report/shale-gas-and-tight-oil-boom/ (accessed Feburary 16, 2019).

Chen, Z., Osadetz, K.G., Jiang, C., Li, M., 2009. Spatial variation of Bakken or Lodgepole oils in the Canadian Williston Basin. AAPG Bulletin. 93, 829-851. https://doi.org/10.1306/03160908120

Clarkson, C.R., Freeman, M., He, L., Agamalian, M., Melnichenko, Y.B., Mastalerz, M., Bustin, R.M., Radliński, A.P., Blach, T.P., 2012. Characterization of tight gas reservoir pore structure using USANS/SANS and gas adsorption analysis. Fuel 95, 371-385. https://doi.org/10.1016/j.fuel.2011.12.010

Clarkson, C.R., Solano, N., Bustin, R.M., Bustin, A.M.M., Chalmers, G.R.L., He, L., Melnichenko, Y.B., Radliński, A.P., Blach, T.P., 2013. Pore structure characterization of North American shale gas reservoirs using USANS/SANS, gas adsorption, and mercury intrusion. Fuel 103, 606-616. https://doi.org/10.1016/j.fuel.2012.06.119

Day-Stirrat, R.J., Aplin, A.C., Środoń, J., van der Pluijm, B.A., 2008. Diagenetic reorientation of phyllosilicate minerals in Paleogene mudstones of the Podhale Basin, Southern Poland. Clays Clay Miner. 56, 100-111. https://doi.org/10.1346/CCMN.2008.0560109

Davudov, D., Moghanloo, R.G., 2018. Scale-dependent pore and hydraulic connectivity of shale matrix. Energy & Fuels 32, 99-106. https://doi.org/10.1021/acs.energyfuels.7b02619

Drillinginfo, 2017. https://info.drillinginfo.com/ (accessed Feburary 16; 2019).

Fishman, N.S., Egenhoff, S.O., Boehlke, A.R., Lowers, H.A., 2015. Petrology and diagenetic history of the upper shale member of the Late Devonian-Early Mississippian Bakken Formation, Williston Basin, North Dakota. GSA Special Papers. 515, 125-151. https://doi.org/10.1130/2015.2515(07)

Gao, Z., Hu, Q., 2013. Estimating permeability using median pore-throat radius obtained from mercury intrusion porosimetry. J. Geophys. Eng. 10, 025014. https://doi.org/10.1088/1742-2132/10/2/025014

Gao, Z., Hu, Q., 2015. Gas diffusivity in porous media: Determination by mercury intrusion porosimetry and correlation to porosity and permeability. J. Porous Media 18, 1231-1238. https://doi.org/10.1615/JPorMedia.v18.i12.60

Gao, Z., Hu, Q., Liang, H., 2013. Gas diffusivity in porous media: Determination by mercury intrusion porosimetry and correlation to porosity and permeability. J. Porous Media 16, 607-617. https://doi.org/10.1615/JPorMedia.v16.i7.30

Gu, X., Cole, D.R., Rother, G., Mildner, D.F.R., Brantley, S.L., 2015. Pores in Marcellus Shale: A neutron scattering and FIB-SEM study. Energy and Fuels 29, 1295-1308. https://doi.org/10.1021/acs.energyfuels.5b00033

Hall, P.L., Mildner, D.F.R., Borst, R.L., 1986. Small-angle scattering studies of the pore spaces of shaly rocks. J. Geophys. Res. 91, 2183. https://doi.org/10.1029/JB091iB02p02183

Hinde, A.L., 2004. PRINSAS - A Windows-based computer program for the processing and interpretation of small-angle scattering data tailored to the analysis of sedimentary rocks. J. Appl. Crystallogr. 37, 1020-1024. https://doi.org/10.1107/S0021889804021260

Hu, Q., Ewing, R.P., Dultz, S., 2012. Low pore connectivity in natural rock. J. Contam. Hydrol. 133, 76-83. https://doi.org/10.1016/j.jconhyd.2012.03.006

Hu, Q., Zhang, Y., Meng, X., Li, Z., Xie, Z., Li, M., 2017. Characterization of micro-nano pore networks in shale oil reservoirs of Paleogene Shahejie Formation in Dongying Sag of Bohai Bay Basin, East China. Pet. Explor. Dev. 44, 720-730. https://doi.org/10.1016/S1876-3804(17)30083-6

Jin, H., Sonnenberg, S.A., 2013. Characterization for source rock potential of the Bakken Shales in the Williston Basin, North Dakota and Montana, in: Unconventional Resources Technology Conference, Denver, Colorado, 12-14 August 2013. Society of Exploration Geophysicists, American Association of Petroleum Geologists, Society of Petroleum Engineers, pp. 117-126. https://doi.org/10.1190/urtec2013-013

Jin, H., Sonnenberg, S.A., 2012. Source sock potential of the Bakken Shales in the Williston Basin , North Dakota and Montana: AAPG Search and Discovery Article No. 20156.

Katz, A.J., Thompson, A.H., 1985. Fractal sandstone pores: Implications for conductivity and pore formation. Phys. Rev. Lett. 54, 1325-1328. https://doi.org/10.1103/PhysRevLett.54.1325

King, H.E., Eberle, A.P.R., Walters, C.C., Kliewer, C.E., Ertas, D., Huynh, C., 2015. Pore architecture and connectivity in gas shale. Energy and Fuels 29, 1375-1390. https://doi.org/10.1021/ef502402e

Kline, S.R., 2006. Reduction and analysis of SANS and USANS data using IGOR Pro. J. Appl. Crystallogr. 39, 895-900. https://doi.org/10.1107/S0021889806035059

Ko, L.T., Loucks, R.G., Ruppel, S.C., 2017. Origin and characterization of Eagle Ford pore networks in the south Texas Upper Cretaceous shelf. AAPG Bulletin. 3, 387-418. https://doi.org/10.1306/08051616035

Kowalski, B.L., Sonnenberg, S.A., 2011. Mineralogic Analysis of the Middle Bakken Member, Parshall Field Area, Mountrail County, North Dakota, in: The Bakken-Three Forks Petroleum System in the Williston Basin. pp. 102-126.

Krohn, C.E., 1988. Sandstone fractal and Euclidean pore volume distributions. J. Geophys. Res. 93, 3286-3296. https://doi.org/10.1029/JB093iB04p03286

Kuhn, P.P., Di Primio, R., Hill, R., Lawrence, J.R., Horsfield, B., 2012. Three-dimensional modeling study of the low-permeability petroleum system of the Bakken Formation. AAPG Bulletin. 96, 1867-1897. https://doi.org/10.1306/03261211063

Lake, J.A., 1967. An iterative method of slit-correcting small angle X-ray data. Acta Crystallogr. 23, 191-194. https://doi.org/10.1107/S0365110X67002440

LeFever, J.A., Martiniuk, C.D., Dancsok, E.F.R., Mahnic, P.A., 1991. Petroleum potential of the middle member, Bakken Formation, Williston Basin, in: Sixth International Williston Basin Symposium. pp. 74–94.

LeFever, J., 2008. Bakken Formation map series: North Dakota Geological Survey, scale 1:1,000,000, 5 sheets.

Liu, K., Ostadhassan, M., Zhou, J., Gentzis, T., Rezaee, R., 2017. Nanoscale pore structure characterization of the Bakken shale in the USA. Fuel 209, 567-578. https://doi.org/10.1016/j.fuel.2017.08.034

Loucks, R., Reed, R., Ruppel, S., 2009. Morphology, genesis, and distribution of nanometer-scale pores in siliceous mudstones of the Mississippian Barnett Shale. J. Sediment. Res. 79, 848-861. https://doi.org/10.2110/jsr.2009.092

Loucks, R.G., Reed, R.M., Ruppel, S.C., Hammes, U., 2012. Spectrum of pore types and networks in mudrocks and a descriptive classification for matrix-related mudrock pores. AAPG Bulletin. 96, 1071-1098. https://doi.org/10.1306/08171111061

McNaught, A. D., and Wilkinson, A., 1997. Compendium of chemical terminology: IUPAC Recommendations, 2nd ed., Blackwell, Malden.

Madden, A.S., Hochella, M.F., Luxton, T.P., 2006. Insights for size-dependent reactivity of hematite nanomineral surfaces through Cu^{2+} sorption. Geochim. Cosmochim. Acta 70, 4095-4104. https://doi.org/10.1016/j.gca.2006.06.1366

Melnichenko, Y.B., 2016. Small-angle Scattering from Confined and Interfacial Fluids. Springer. https://doi.org/10.1007/978-3-319-01104-2

Nordeng, S.H., 2009. The Bakken Petroleum System: An Example of a Continuous Petroleum Accumulation. North Dakota Dep. Miner. Resour. Newsl. 36, 21-24.

Passey, Q.R., Bohacs, K., Esch, W.L., Klimentidis, R., Sinha, S., 2010. From oil-prone source rock to gas-producing shale reservoir - geologic and petrophysical characterization of unconventional shale gas reservoirs, in: International Oil and Gas Conference and Exhibition in China. Society of Petroleum Engineers. https://doi.org/10.2118/131350-MS

Patterson, R., 2016. Bakken Oil Production Soars After Long Decline. http://oilprice.com/Energy/Crude-Oil/Bakken-Oil-Production-Soars-After-Long-Decline.html/ (accessed by Feburary 16, 2019).

Pitman, J.K., Price, L.C., LeFever, J. a, 2001. Diagenesis and fracture development in the Bakken Formation, Williston Basin: Implications for reservoir quality in the middle member. U.S. Department of the Interior, U.S. Geological Survey. https://doi.org/10.3133/pp1653

Porod, G., 1952. Die Röntgenkleinwinkelstreuung von dichtgepackten kolloiden Systemen: Colloid & Polymer Science. 125, 51-57.

Radliński, A.P., Radlińska, E.Z., Agamalian, M., Wignall, G.D., Lindner, P., Randl, O.G., 1999. Fractal geometry of rocks. Phys. Rev. Lett. 82, 3078-3081. https://doi.org/10.1103/PhysRevLett.82.3078

Radliński, A.P., Boreham, C.J., Lindner, P., Randl, O., Wignall, G.D., Hinde, A., Hope, J.M., 2000. Small angle neutron scattering signature of oil generation in artificially and naturally matured hydrocarbon source rocks. Org. Geochem. 31, 1-14. https://doi.org/10.1016/S0146-6380(99)00128-X

Radlinski, A.., Mastalerz, M., Hinde, A.., Hainbuchner, M., Rauch, H., Baron, M., Lin, J.., Fan, L., Thiyagarajan, P., 2004. Application of SAXS and SANS in evaluation of porosity, pore size distribution and surface area of coal. Int. J. Coal Geol. 59, 245-271. https://doi.org/10.1016/j.coal.2004.03.002

Radlinski, A.P., 2006. Small-Angle Neutron Scattering and the Microstructure of Rocks. Rev. Mineral. Geochemistry 63, 363-397. https://doi.org/10.2138/rmg.2006.63.14

Ruppert, L.F., Sakurovs, R., Blach, T.P., He, L., Melnichenko, Y.B., Mildner, D.F.R., Alcantar-Lopez, L., 2013. A USANS/SANS study of the accessibility of pores in the Barnett Shale to methane and water. Energy & Fuels 27, 772-779. https://doi.org/10.1021/ef301859s

Schmidt, P.W., 1982. Interpretation of small-angle scattering curves proportional to a negative power of the scattering vector. J. Appl. Crystallogr. 15, 567-569. https://doi.org/10.1107/S002188988201259X

Simenson, A.L., Sonnenberg, S.A., Cluff, R.M., 2011. Depositional facies and petrophysical analysis of the Bakken Formation, Parshall Field and surrounding area, Mountrail County,

North Dakota, in: The Bakken-Three Forks Petroleum System in the Williston Basin. pp. 48-101.

Slatt, R.M., O'Brien, N.R., 2011. Pore types in the Barnett and Woodford gas shales: Contribution to understanding gas storage and migration pathways in fine-grained rocks. AAPG Bulletin. 95, 2017-2030. https://doi.org/10.1306/03301110145

Slatt, R.M., O'Brien, N., Molinares-Blanco, C., Serna-Bernal, A., Torres, E., Philp, P., 2013. Pores, spores, pollen and pellets: Small, but significant constituents of resource shales, in: Unconventional Resources Technology Conference, Denver, Colorado, 12-14 August 2013. Society of Exploration Geophysicists, American Association of Petroleum Geologists, Society of Petroleum Engineers, pp. 630-642. https://doi.org/10.1190/urtec2013-065

Smith, M.G., Bustin, R.M., 1998. Production and preservation of organic matter during deposition of the Bakken Formation (Late Devonian and Early Mississippian), Williston Basin. Palaeogeogr. Palaeoclimatol. Palaeoecol. 142, 185-200. https://doi.org/10.1016/S0031-0182(98)00063-7

Sonnenberg, S.A., Pramudito, A., 2009. Petroleum geology of the giant Elm Coulee field, Williston Basin. AAPG Bulletin. 93, 1127-1153. https://doi.org/10.1306/05280909006

Sweeney, J.J., Braun, R.L., Burnham, A.K., Gosnold, W.D., 1992. A chemical kinetic model of hydrocarbon generation from the Bakken Formation, Williston Basin, North Dakota.

Thomas, J.J., Valenza, J.J., Craddock, P.R., Bake, K.D., Pomerantz, A.E., 2014. The neutron scattering length density of kerogen and coal as determined by CH_3OH/CD_3OH exchange. Fuel 117, 801-808. https://doi.org/10.1016/j.fuel.2013.09.075

Thompson, A., 1991. Fractals in rock physics. Annu. Rev. Earth Planet. Sci. 19, 237-262. https://doi.org/10.1146/annurev.earth.19.1.237

U.S. Energy Information Administration (EIA), 2017. How much shale (tight) oil is produced in the United States? https://www.eia.gov/tools/faqs/faq.php?id=847&t=6/ (accessed by Feburary 16, 2019).

Vineyard, G.H., 1954. Multiple scattering of neutrons. Phys. Rev. 96, 93-98. https://doi.org/10.1103/PhysRev.96.93

Wang, S., Javadpour, F., Feng, Q., 2016. Confinement correction to mercury intrusion capillary Ppressure of shale nanopores. Sci. Rep. 6, 20160. https://doi.org/10.1038/srep20160

Washburn, E.W., 1921. The dynamics of capillary flow. Phys. Rev. 17, 273-283. https://doi.org/10.1103/PhysRev.17.273

Webb, P.A., 2001. An introduction to the physical characterization of materials by mercury intrusion porosimetry with emphasis on reduction and presentation of experimental data. Micromeritics Instrument Corp, Norcross, Georgia.

Webster, R., 1984. Petroleum source rocks and stratigraphy of the Bakken Formation in North Dakota, in: Hydrocarbon Source Rocks of the Greater Rocky Mountain Region. pp. 57-81.

Yang, R., He, S., Hu, Q., Sun, M., Hu, D., Yi, J., 2017. Applying SANS technique to characterize nano-scale pore structure of Longmaxi shale, Sichuan Basin (China). Fuel 197, 91-99. https://doi.org/10.1016/j.fuel.2017.02.005

Zhao, J., Jin, Z., Hu, Q., Jin, Z., Barber, T.J., Zhang, Y., Bleuel, M., 2017. Integrating SANS and fluid-invasion methods to characterize pore structure of typical American shale oil reservoirs. Sci. Rep. 7, 15413. https://doi.org/10.1038/s41598-017-15362-0

Chapter 3: Mineral-controlled nm-µm-scale pore structure of saline lacustrine shale in Qianjiang Depression, Jianghan Basin, China

Yuxiang Zhang[1,2], Qinhong Hu[1,2 *], Shengxiang Long[1], Jianhua Zhao[3], Nyujia Peng[4], Haitao Wang[1], Xiang Lin[4], and Mengdi Sun[4]

[1] State Key Laboratory of Shale Oil and Gas Enrichment Mechanisms and Effective Development, Research Institute of Petroleum Exploration and Production, Sinopec, Beijing 100083, China

[2] Department of Earth and Environmental Sciences, The University of Texas at Arlington, 500 Yates Street, Arlington, TX 76019, USA

[3] School of Geosciences, China University of Petroleum (East China), Qingdao, 266580, China

[4] Faculty of Earth Resources, China University of Geosciences, Wuhan 430074, China

Marine and Petroleum Geology

*Corresponding author:

Qinhong Hu, E-mail address: water19049@gmail.com

Abstract

The pore structure of the saline lacustrine shales in the E*q*3 unit of the Qianjiang Formation was characterized for pore space of μm-nm scales through a combined study of mercury injection capillary pressure (MICP) and small/ultra-small angle neutron scattering (SANS and USANS). X-ray diffraction (XRD) and total organic carbon (TOC) content tests, as well as field emission-scanning electron microscopy (FE-SEM) imaging, are also employed to obtain the mineralogical composition, organic richness, as well as the general pore types and sizes of the selected Qianjiang shale samples. In these samples, three major rock types are identified: (1) silica-rich carbonate mudstone; (2) carbonate/siliceous mudstone; and (3) salt. The porosity, as well as pore size and pore-throat size distributions, generated from both SANS/USANS and MICP techniques indicate a porous rock matrix and well-connected pore networks in the two mudstone rock types. Meanwhile, an averaged TOC of around 3.5 wt.% for E*q*3 unit exhibits a good quality for oil generation potential. This study primarily provides new insights into the pore structure of the Qianjiang shales across a wide measurable range for both pore and pore-throat sizes, and correlates the pore structure and mineral compositions at different scales.

1. Introduction

The Upper Eocene Qianjiang Formation in the Qianjiang Depression, a central part of the Jianghan Basin in Hubei Province of China (Figure 1a) has been attracting an increasing number of geological researches on the saline lacustrine shale and its production (e.g., Wang et al., 2004 a, b; Wu et al., 2013; Hou et al., 2017; Li et al., 2018). Formed in a Creataceous-Eocene orogenic event (Chen, 2007; Wu et al., 2013), the Qianjiang Depression covers an area of approximately 4500 km^2 (Hou et al., 2017), and has an approximately 4-km thick hypersaline sediments consisting of four major units: E*q*1, E*q*2, E*q*3, and E*q*4 (Figure 2; Li et al., 2018). The lacustrine sediments were deposited in the period of two structural cycles (Philp et al., 1989) during which salt was formed with two depressional events (Grice et al., 1998). The sediments compose of hundreds of cyclotherms of alternating salt and mudstone (or sandstone) (Grice et al., 1998; Chen et al., 2002; Fang et al., 2003; Zheng, 2010; Li et al., 2018). Each cyclotherm is a mixture of organic-rich siliciclastic/carbonate mudstones with an overlying and an underlying sheet-like salt layer, and thus, forming individual self-sourced petroleum systems (Wang et al., 2004; Li et al., 2018). The expelled hydrocarbons can probably only migrate laterally through the mudstone or sand layers, or be retained in the mudstones as the salt layers effectively prevent the flow of hydrocarbons in the vertical direction (Liu et al., 2010; Zheng, 2010; Hou et al., 2017). It is important to study the E*q*3 unit as the oil production in the Qianjiang Depression primarily comes from mature source rocks in the E*q*3/E*q*4 units of the Qianjiang Formation (Peters et al., 1996; Hou et al., 2017).

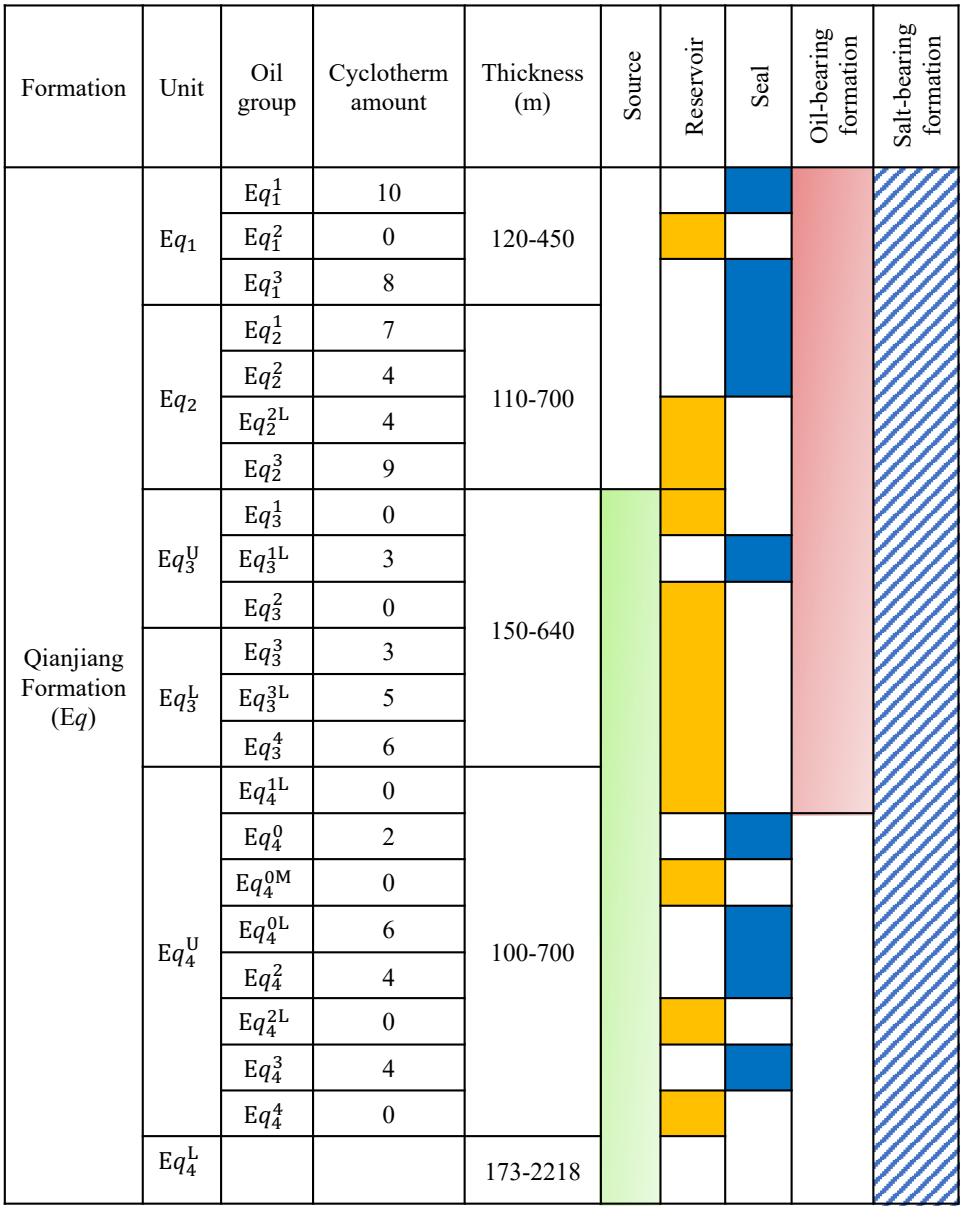

Figure 2. Stratigraphic column showing the unit, oil group, cyclotherm amount, thickness, source rock, reservoir rock, seal, oil-bearing and salt-bearing formations of the Qianjiang Formation (modified from Ulmishek, 1992; Li et al., 2012; Huang and Hinnov, 2014)

The study samples come from the E*q*3 unit of the Qianjiang Formation in the Wangchang Oilfield, which is the first, as well as the largest, oil field discovered in Qianjiang Depression

with the oil primarily trapped in sandstones (Ulmishek, 1992). With the advances in horizontal drilling and fracturing techniques, the thin layered mudstones in the E*q*3 unit have become one of the new targets for recent drilling in this area. Previous studies reported that E*q*3 unit has low-to-medium mature source rocks (Type I, II kerogen; not particularly high TOC content) (Guo et al., 2012; Wang et al., 2011; Hou et al., 2017) with an average porosity of 10.2-20.4% and permeability of 29.2-430 mD (Guo et al., 2012). However, more detailed laboratory-based pore structure characterization of core samples in this area are not available. Therefore, our investigations employ two complementary techniques, SANS/USANS (small/ultra-small angle neutron scattering) and MICP (mercury injection capillary pressure), to characterize μm- to nm-scale pore networks in the Qianjiang lacustrine shale samples.

Over the past ten years, SANS and USANS have proved to be powerful techniques for characterizing nanopore structure of the sedimentary rocks (e.g., sandstone, carbonates, coal) due to their capabilities of yielding nm-μm-scale pore structure information (Radlinski et al., 2004; Mastalerz et al., 2012; Anovitz and Cole, 2015; Bahadur et al., 2016; Sakurovs et al., 2017; Zhao et al., 2017; Sun et al., 2018). Considering the increasing interest in low-permeable media, the (U)SANS technique has been more frequently utilized to study tight rocks such as oil/gas shales (Hall et al., 1986; Radlinski et al., 2000; Clarkson et al., 2012; Ruppert et al., 2013; Bahadur et al., 2014; Gu et al., 2015; King et al., 2015; Yang et al., 2017; Blach et al., 2017; Sun et al., 2018). The advantages of combined SANS and USANS study include: (1) the ability to cover a broad pore size spectrum from ~1 nm to 20 μm (Figure 3); (2) the ability to measure the real total porosity (both accessible and inaccessible porosity); and (3) the non-destructive nature of the experiments (Clarkson et al., 2012).

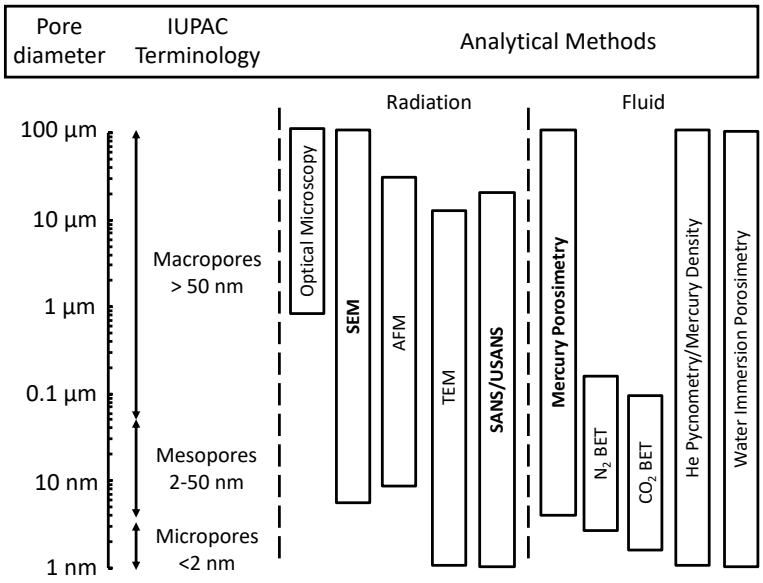

Figure 3. Multiple analytical methods used to acquire pore space information from rock samples (modified from Anovitz and Cole, 2015). Three techniques (bold fonts) are employed in this work to study the effect of mineral-controlled pore type on porosity and pore (throat) size distribution.

More accessible than (U)SANS facilities, MICP is a commonly used technique in the oil and gas industry to characterize porous media (e.g., mudstone samples) and obtain pore structure characteristics across a full pore-throat size range (e.g., Webb, 2001; Gao et al., 2013). Unlike (U)SANS, MICP technique only measures pore-throat controlled pore spaces which are accessible to the sample surface, with a minimum detectable pore-throat size of ~3 nm. Therefore, a combined study of (U)SANS and MICP, assisted with field emission-scanning electron microscopy (FE-SEM) imaging, enables us to acquire a holistic information of pore structure across the micropore- to macropore-scales (Figure 3).

Our specific research objectives are to: (1) evaluate and compare the porosity, pore (throat) size distribution in different oil groups and salt layers; and (2) investigate the controlling effect of mineral compositions on pore structure of Qianjiang lacustrine shale.

2. Experiments

2.1 Sample preparation and composition analysis

In this study, nine core samples were acquired from two drilled wells, WY11 and W4, located in the Wangchang Oilfield (Figure 1b; Table 1). The core samples were subsampled and prepared into multiple sizes for the following laboratory tests: (1) large fragmental pieces (~0.5-1 cm) for MICP analysis; (2) thin slabs (~5 mm×10 mm×10 mm) for FE-SEM imaging; (3) wafers (cut parallel to the shale lamination) with a radius of ~1 cm and a thickness of ~750 μm for SANS/USANS measurements; (4) grains with a particle size of 177-500 μm (#35/80 mesh) for SANS/USANS measurements; and (5) pulverized powders for XRD (X-ray diffraction) and TOC (total organic carbon) tests.

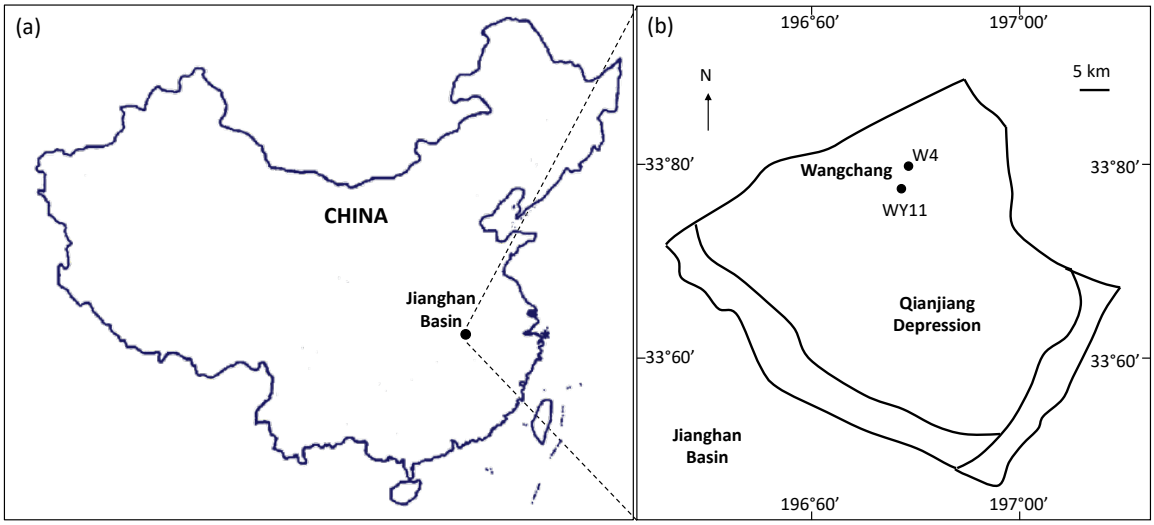

Figure 1. Map of Qianjiang Depression in Jianghan Basin and well locations of WY11 and W4 from which core samples are studied in this work (modified from Wang et al., 2004)

Table 1. Basic information of lacustrine Qianjiang Formation samples used in this work

Sample ID	Depth (m)	Oil Group	Mineralogy, wt.%				TOC, wt.%
			QFM	Carbonate	Clay	Salt	
WY11-1581	1581.43	E*q*3^{3}-3	24.3	57.7	2.9	-	4.37
WY11-1633	1633.04	E*q*3^{3L}-6	33.9	49.9	5.0	-	5.05
WY11-1634	1634.58	E*q*3^{3L}-6	6.6	81.1	1.1	-	3.08
WY11-1648	1648.31	E*q*3^{3L}-7	15.4	73.9	6.6	-	2.57
WY11-1748	1748.45	E*q*3^{4L}-12	N/A	N/A	N/A	N/A	2.05
W4-1763	1763.8	N/A	-	-	-	100	N/A
W4-1771	1771.3	E*q*3^{4L}-10	22.6	36.9	21.0	-	3.75
W4-1774	1774.3	E*q*3^{4L}-10	28.3	27.1	18.1	-	2.15
W4-1785	1785.73	N/A	-	-	-	100	N/A

QFM: quartz, feldspar, and mica.

Hyphen (-) indicates that the mineral is not detected in the sample.

N/A indicates that either the information or data are not available

The analyses of mineral compositions and TOC contents are critical to understand the dominant minerals and organic matter richness in the shale, as well as their controls on the pore structure. The XRD test was performed using the MAXima X XRD-7000 X-Ray Diffractometer (Shimadzu) which enables a fast measurement and data collection of samples operated with the standard Cu X-ray tube at a rotation angle of 2-70°. The qualitative and quantitative analyses of

the minerals are identified (~1% error) using the RDB-Mineral database. The TOC measurement was conducted by combining the SSM-5000A Solid Sample Combustion Unit with the TOC-Vws Analyzer (Shimadzu), and the value is calculated by subtracting the IC (inorganic carbon; with a method of catalytically-aided combustion oxidation at 900°C) from the TC (total carbon; with a method of pre-acidification and combustion oxidation at 250°C) contents. In FE-SEM work, thin slabs of the samples were polished to a level surface, milled by argon-ion, and mounted onto SEM stubs with carbon paste to provide a conductive surface. Afterwards, the sample images were collected at an acceleration voltage of 5 kV at a working distance of 4-6 meters using Merlin Compact (Zeiss Microscopy).

2.2 MICP experiments

MICP analyses were performed using a mercury porosimeter (AutoPore IV 9500, Micromeritics) for all nine samples. The studied samples were prepared following the procedures reported in Gao and Hu (2015), and then put into a penetrometer and subjected to progressively increased pressures from 0.2 psi (0.001 MPa) to 55,000 psi (380 MPa). The non-wetting mercury was driven into the pore networks, by the applied high pressure to overcome the capillary pressure, and intrude into increasingly smaller connected pore spaces. Information of bulk density, total pore volume, total pore surface area, and porosity as well as pore-throat size distribution can be obtained (Webb, 2001) through a single run. The pore-throat size is determined by the Washburn Equation (Washburn, 1921)

$$D = -\frac{4\gamma \cos \theta_c}{P} \quad (1)$$

based on the assumption of using constant sample surface tension (γ = 485 dyne cm^{-1}) and constant mercury contact angle (θ_c = 130º), and variable applied pressure *P* (dyne cm^{-2}) from the instrument. However, a recent work indicated that the contact angle of mercury increases as the pore size decreases (Wang et al., 2016), and therefore, a corrected Washburn equation with variable contact angle and surface area as a function of pore throat size is employed, which derive the measurable pore-throat size range from 3 nm to about 1 mm in this study. In addition, Katz and Thompson's method (1986; 1987)

$$K = \frac{1}{89}\frac{L_{max}^3}{L_t}\emptyset S_{L_{max}} \quad (2)$$

was adopted to derive the permeability from MICP data, and details are provided in the work of Gao and Hu (2013).

2.3 Neutron scattering experiments

2.3.1 Sample preparation and (U)SANS data collection

Three out of nine samples (i.e., WY11-1634, WY11-1648, and Wang4-1774) were prepared for (U)SANS experiments. As mentioned in Section 2.1, two sample sizes, wafer (~750 μm thick) and grains (a particle size of 177-500 μm), were used. Wafers for all three samples were prepared by cutting and polishing the samples parallel to the bedding orientation, and then attached to the cadmium plates with a circular aperture of 3/8 inches (~9.5 mm). By doing so, the neutron beam is perpendicular to the bedding plane during scattering, and the isotropic pore structure information will be obtained (Gu et al., 2015). Samples WY11-1634 and Wang4-1774 were also crushed for only a few seconds for disaggregation with a minimal disturbance to its

pore structure, size fractions of grains at 177-500 μm were loaded into demountable titanium cells, which have a circular aperture of 0.75'' (1.905 cm) and a path length of ~0.5 mm. The purpose of using granular samples is to collect the pore structure information from an averaged all orientations rather than just a single direction (Bahadur et al., 2014).

In this study, both SANS and USANS measurements were carried out at the NIST Center for Neutron Research using the NG7-30m SANS instrument and BT5 perfect crystal diffractometer USANS instrument (Barker et al., 2005), respectively. SANS data were collected at sample-to-detector distances of 1 m, 4 m, 13 m (and with lens) covering a Q-range from 0.001 $Å^{-1}$ to around 0.4 $Å^{-1}$ with a wavelength (λ) of 6.0 Å (8.09 Å at the 13-m lens). The USANS data were collected to cover a Q range from 2.5×10^{-5} $Å^{-1}$ - 0.001 $Å^{-1}$, using a wavelength of 2.4 Å. The scattering vector is expressed as

$$Q = 4\pi\lambda^{-1}\sin\theta \tag{3}$$

where λ is the wavelength of the neutron beam, and 2θ is the scattering angle. The intensity of scattered neutrons $I(Q)$ comes from pores, and $I(Q)$ is proportional to $(\Delta\rho)^2$, the square of the difference between the scattering length density (SLD) of the scattering objects (i.e., pores) and its surrounding medium (Melnichenko, 2016). The averaged SLD of the sample is calculated using

$$\rho_{matrix} = \sum_{i=1}^{n} \phi_i \rho_i \tag{4}$$

where ϕ_i and ρ_i are the volume fraction and SLD of each component in the rock matrix, respectively.

2.3.2 (U)SANS data reduction

The collected SANS data were reduced to an absolute scale and combined with desmeared USANS data (Lake, 1967), using NIST data reduction macros (Kline, 2006), to cover a wide Q-range from about 2.5×10^{-5} Å^{-1} to 0.4 Å^{-1}. The radius R of the pores can be calculated as $R \approx 2.5/Q$ (Radlinski, 2000).

We further utilized TNNLS tool in the Irena macros (Ilavsky, 2009) to calculate porosity and generate pore-size distribution in the measurable size ranges of 1 nm to 20 μm. As the pore morphology in the selected samples can be described as a polydisperse spherical pore network (see Section 3.1), and therefore, we employed a polydisperse size-distribution model (PDSM) to analyze the data. The scattering intensities in this PDSM can be expressed as Equation 5 (King et al., 2015):

$$I(Q) = (\rho_1 - \rho_2)^2 \sum P(Q,R)^2 F(r) V(r)^2 N \Delta r \quad (5)$$

where ρ_1 and ρ_2 are the SLD_S of pores and their surrounding medium; $V_r = (4/3)\pi r^3$ is the volume for a sphere with radius r; and $P(Q,R)$ is the form factor (King et al., 2015).

3. Results and Discussion

3.1 Sample composition

The mineralogical composition and TOC content, together with geological background information, of Qianjiang samples are listed in Table 1. Samples from five oil groups (i.e., E$q3^3$-3, E$q3^{3L}$-6, E$q3^L$-7, E$q3^{4L}$-12) in WY11 well primarily compose of carbonates (49.9-81.8 wt.%;

mainly dolomites) and have a low clay content (1.1-6.6 wt.%) but a relatively high TOC value (2.57-5.05 wt.%). According to the classification of mudstone (Gamero-Diaz and Miller, 2012), these samples can be classified as silica-rich carbonate mudstones. In W4 well, two samples (W4-1771 and W4-1774) belong to E$q3^{4L}$-10 oil group. Compared with samples in WY11 well, these two samples have a higher clay content (18.1-21.0 wt.%) and a lower carbonate content (27.1-36.9 wt.%), and therefore being classified as silica-rich carbonate mudstones. Another two samples in W4 well, i.e., W4-1763 and W4-1785, are identified as salts (100 wt.% halite) which should be collected from salt layers overlying and underlying the E$q3^{4L}$-10 oil group.

To calculate the averaged SLD for each sample in (U)SANS analyses, the specific mineral components, and their corresponding mineral types and $SLDs$ are given in Table 2. The volume fraction of each component is normalized based on the weight percentage of every single mineral and TOC content. The computed SLD values of WY11-1634 and WY11-1648 are quite close (4.80 and 4.82×10^{10} cm^{-2}) due to a similarity in mineral composition, while W4-1774 has a lower SLD value (3.81×10^{10} cm^{-2}) as a result of a lower proportion of carbonates.

Considering the similarity of mineral compositions in these samples, we only selected WY11-1634 and W4-1774 to represent the rest of the samples, in addition to salt samples. Overall observations of the FE-SEM images (Figure 4) indicate that both WY11-1634 and W4-1774 are very porous with massive μm-scale pores (> 1 μm) and nanopores (< 1 μm). The difference is that sample WY11-1634 has many intra-particle pores (particularly dissolved pores) in dolomites (Figs. 4a-c), while W4-1774 has more clay-related pores (Figs. 4d-f) and micro-fractures (Fig. 4d). Though these samples have moderate TOC contents, organic matter is not widely distributed (Fig. 4f).

Table 2. Mineral component, type, scattering length density, normalized weight and volume percentages for three (U)SANS samples.

Component	Type	SLD_i ($\times 10^{10}$ cm^{-2})	WY11-1634		WY11 1648		W4-1774	
			Wt.%	*Vol.%*	*Wt.%*	*Vol.%*	*Wt.%*	*Vol.%*
Quartz	QFM	4.18	4.65	4.78	10.43	10.75	10.76	10.69
Albite	QFM	3.96	0	0	4.58	4.78	12.72	12.78
Enstatite	QFM	1.85	1.74	1.49	0	0	4.21	3.46
Pyrite	Sulfide	3.81	0	0	0	0	4.99	2.62
Anhydrite	Sulfate	3.52	0	0	0	0	3.03	2.69
Gypsum	Sulfate	2.26	0.97	1.12	0	0	2.94	3.27
Calcite	Carbonate	4.69	0.58	0.58	0	0	14.68	14.25
Dolomite	Carbonate	5.40	57.67	55.33	40.53	38.99	4.11	3.81
Minrecordite	Carbonate	5.38	16.09	12.71	0	0	0	0
Ankerite	Carbonate	5.32	4.26	3.81	31.47	28.19	7.73	6.67
Kutnohorite	Carbonate	4.79	0	0.0	0	0	0	0
Halite	Salt	2.94	9.79	12.35	4.09	5.18	14.87	18.12
Illite	Clay	3.49	0	0	6.43	6.39	16.05	15.36
Muscovite	Clay	3.92	0	0	0	0	1.66	1.62
Glauconite	Clay	4.18	1.07	0.96	0	0	0	0
TOC	Organic matter	3.50	3.08	6.88	2.57	5.76	2.15	4.64
Computed SLD ($\times 10^{10}$ cm^{-2})	-	-	4.80		4.82		3.81	

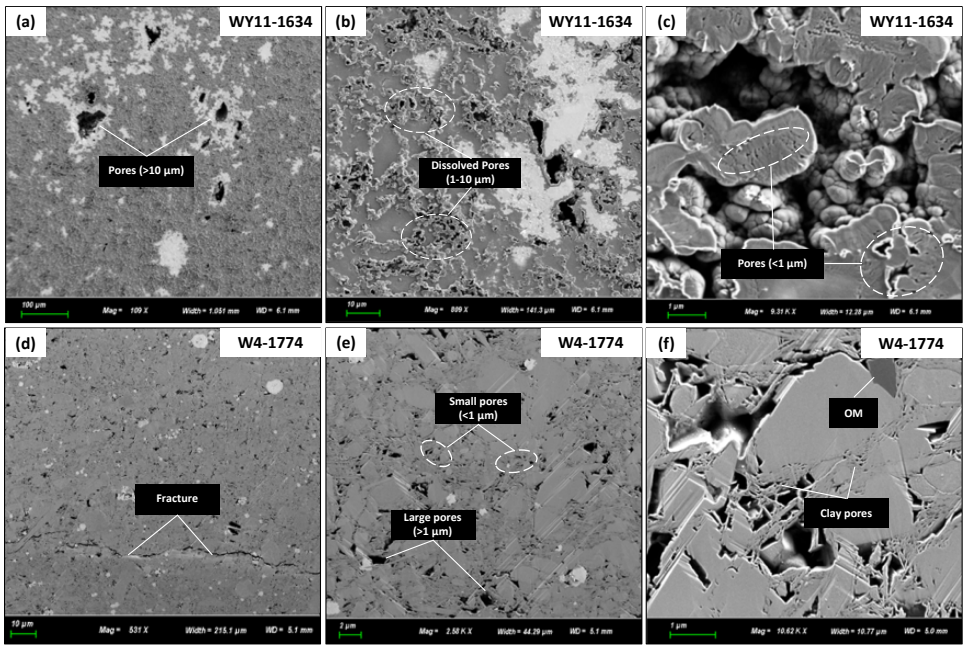

Figure 4. FE-SEM images (a)(b)(c) WY11-1634 and (d)(e)(f) W4-1774 revealing the μm- to nm-sized fractures and mineral pores in two Qianjiang shale samples.

3.2 MICP results

In this study, MICP offers the pore structure characteristics in a detecting size range from about 3 nm to 1 mm. Table 3 shows the results of bulk density, total pore volume, surface area, porosity, and permeability for all samples; In addition, Figure 5 presents the results of pore-throat size distribution. The bulk density varies between 1.73-2.23 g/cm^3 and the porosity of all mudstones is large (7.00-26.8%). Two salt samples have bulk density (2.09-2.11 g/cm^3), porosity (2.64-2.76%) and permeability (0.64-1.30×10^{-2} mD), indicating that they are halite with negligible impurities.

Table 3. MICP-derived pore structure characteristics of all studied samples

Sample	Bulk density (g/cm^3)	Total pore volume (mm^3/g)	Surface area (m^2/g)	Porosity (%)	Permeability (mD)
WY11-1581	1.73	40.4	0.7	7.00	8.73×10^{-4}
WY11-1633	2.17	63.1	3.0	13.68	1.56×10^{-4}
WY11-1634	2.14	79.1	4.7	16.91	0.83×10^{-4}
WY11-1648	1.92	138.8	8.7	26.60	0.15×10^{-4}
WY11-1748	2.23	51.3	4.2	11.45	2.19×10^{-4}
W4-1763	2.11	12.5	2.0	2.64	1.30×10^{-2}
W4-1771	1.88	142.7	9.8	26.82	4.72×10^{-4}
W4-1774	2.10	81.9	13.8	17.21	0.18×10^{-4}
W4-1785	2.09	13.2	1.3	2.76	0.64×10^{-2}

Mineral compositions have a critical influence on the pore structure of Qianjiang lacustrine shale. The silica-rich carbonate mudstone samples in WY11 well have a similar pore-throat size distribution with pore throats centralizing in the range of 20 nm - 1 μm (Fig. 5a). This indicates that the majority of pores, mostly carbonate dissolved ones (Figures 4a-c), are interconnected by pore-throats in this size range. Moreover, these pores and pore-throats together dominate the entire pore system by contributing over 70-90% of the total porosity. The studied samples have high matrix permeabilities, with the differences ranging only within one-order-of-magnitude. In contrast, samples W4-1771 and W4-1774 are carbonate/siliceous mudstones with an averaged high porosity of ~22% and similar matrix permeabilities, as compared to silica-rich carbonate

mudstones. However, the carbonate/siliceous mudstones exhibit a bimodal size distribution (Figure 5b) with pore throats located in two regions: (1) 5 nm to 500 nm; (2) 10 μm to 1 mm. The first region can be considered to be related to small inter-clay platelet pores (see Figure 4f), while the second region is linked to micro-fractures as shown in Figure 4d. Two salt samples, W4-1763 and W4-1785, have a much lower porosity (average: ~2.7%) than the two types of mudstones. Also, their pore-throat size distribution indicates an absence of nanopore system, while the pore volumes at 10 μm - 1 mm is possibly related to the cracks generated during sample processing, which also explains why these two salt samples have a larger permeability.

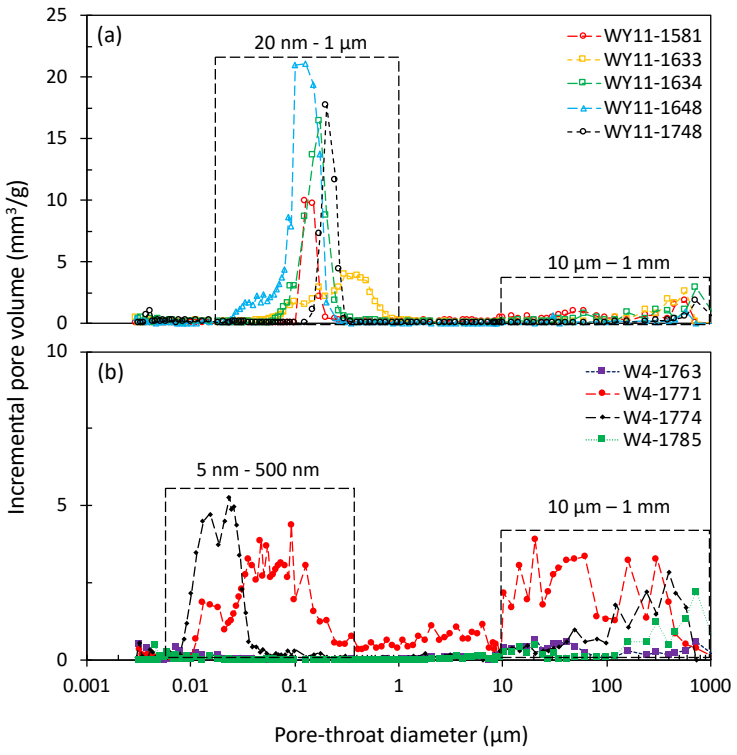

Figure 5. MICP-generated incremental pore volume vs. pore-throat diameter for nine Qianjiang samples in two wells. Results indicate the mudstones in WY11 and W4 wells have different pore-throat size distribution behavior as a result of different mineral composition.

3.3 SANS and USANS results

The combined SANS and USANS profiles are plotted on the log-log scale and shown in Figure 6. The flat background at high-Q (> 0.1 $Å^{-1}$) is considered to be incoherent scattering from hydrogen content in the rock matrix (e.g., organic matter) (Ruppert et al., 2013; Anovitz and Cole, 2015), and will be subtracted in data analyses. The plots indicate two apparent power-law linear relationships in the range of $2.5\times10^{-5} < Q < 4\times10^{-4}$ $Å^{-1}$ and $4\times10^{-4} < Q < 0.1$ $Å^{-1}$. For all five scattering curves, most of the slopes in the former Q-range are close to -2.1, while the slops in the latter Q-range are close to -3.4 (see Figure 6). Therefore, according to previous studies (Bale and Schmidt, 1984; Radlinski et al., 1999; Bahadur, 2016), the fractal dimension D_s ($D_s = 6 + slope$) changes from 3.9 to 2.6, indicating rougher pore surfaces at μm-scale than these at nm-scale.

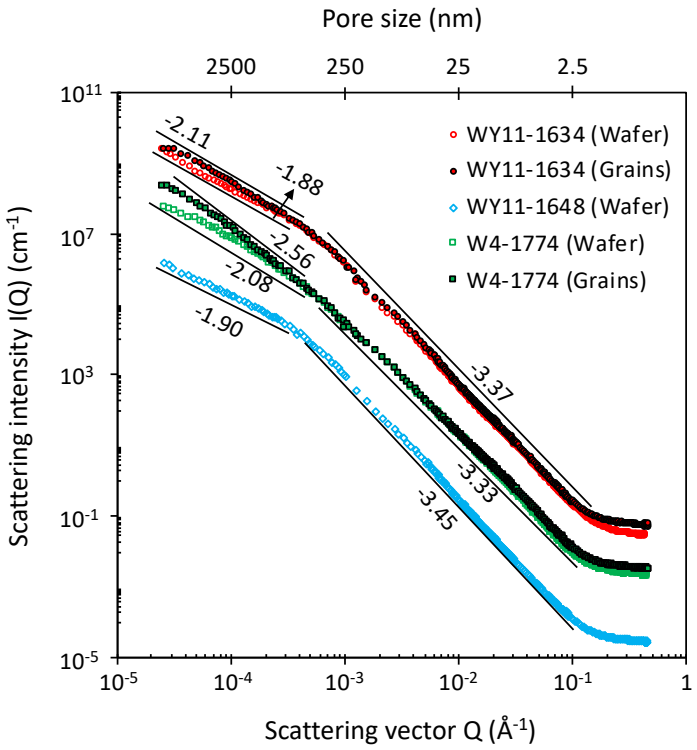

Figure 6. Combined (U)SANS data on the log-log scale with corresponding pore size ranges for tested samples. For clarification and comparison, the scattering curves were shifted vertically by multiply the scattering intensity data by a constant 0.05 for W4-1774, and 0.001 for WY11-1648.

Another observation is that for the same sample, the scattering intensity for grains is overall larger than wafers in the low-Q range (2.5×10^{-5} - 4×10^{-4} Å^{-1}), while their scattering curves are almost overlapped in the Q-range ($4\times10^{-4} < Q < 0.1$ Å^{-1}). There are three possible explanations: (1) an averaged all orientation (grains) creates more contrast, $(\Delta\rho)^2$, than one orientation (wafer) at μm-scale; or (2) the preparation for grains creates micro-fractures/open pores (> 1 μm) in the sample, and thus increases the neutron scattering from large pores while without affecting the scattering from nm-scale pores; and (3) the difference of sample thickness (~750 μm for wafer

vs. 177-500 μm for grains) happens to cross over the dual-connectivity zone separated at ~400 μm from the sample edge, as observed for Barnett shale (Hu et al., 2015).

In data analyses, we reset the lowest Q and changed the Q-range to 5×10^{-5} - 0.4 $Å^{-1}$ to achieve pore information corresponding to a pore size of 1 nm - 10 μm. The calculated total porosities for all selected samples are listed in Table 4, and aided with Figure 7 for visualization and comparison. The large overall porosity (> 8%) verifies the porous rock matrix for these mudstones in two wells, consistent with SEM images (see Fig. 3). Table 4 also presents specific porosities of micropores (<2 nm), mesopores (2-50 nm), and macropores (>50 nm) for each sample, with a plot of pore size distribution given in Figure 8. Results show that macropores dominate the pore system with an averaged proportion of 80.5%. Sample W4-1774 has a larger proportion of micro-/mesopores (> 25%) than WY11-1634 (~16%) and WY11-1648 (~11%) (Fig. 7-8; Table 4). This is possibly caused by a higher percentage of clay minerals in sample W4-1774 which contributes more volumes of micro/mesopores.

Table 4. (U)SANS measured porosity of micropores, mesopores, and macropores and total porosity (%)

Sample ID	Micropore (1 - 2 nm)	Mesopore (2 - 50 nm)	Macropore (50 nm - 10 μm)	Total (1 nm - 10 μm)
WY11-1634 (Wafer)	0.10	1.74	9.69	11.53
WY11-1634 (Grains)	0.28	1.90	11.56	13.74
WY11-1648 (Wafer)	0.14	0.81	7.60	8.55
W4-1774 (Wafer)	0.56	2.66	9.19	12.41
W4-1774 (Grains)	0.73	3.44	10.32	14.49

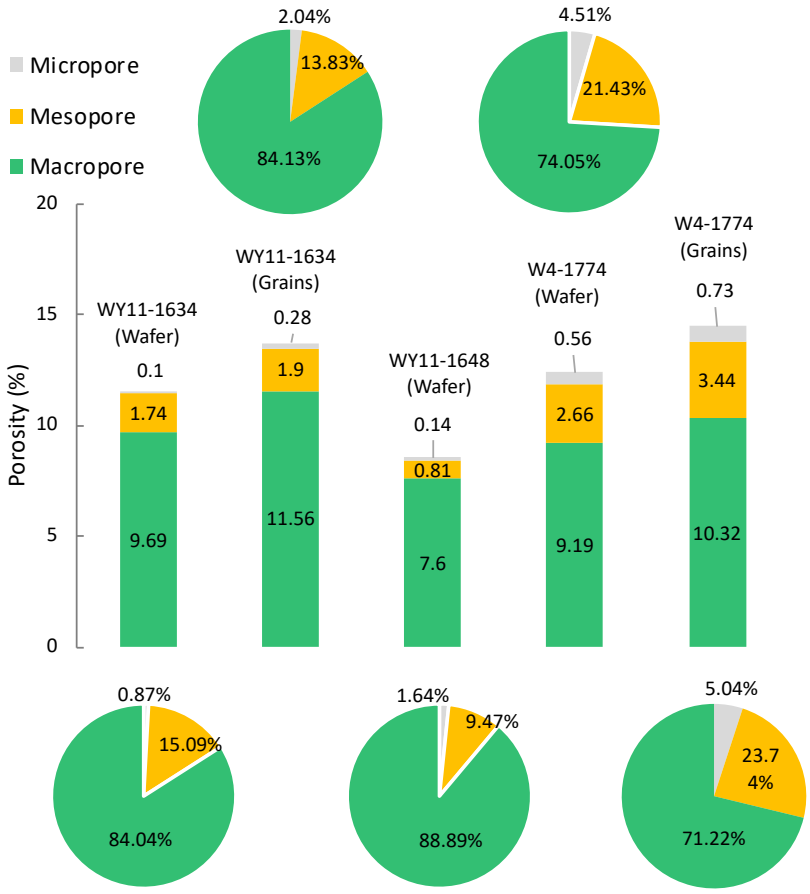

Figure 7. (U)SANS measured porosity of micropore, mesopore, and macropore for three samples (two has both wafers and grains measured) and their corresponding proportions of total porosity.

It is noteworthy that there is no significant difference in the proportion of micropores, mesopores, and macropores in the total porosity when comparing the results of using either a wafer or grains for WY11-1634 and W4-1774 (Figure 7). This indicates that crushed samples with a granular size of 177-500 μm do not cause a further change or damage on pore system smaller than 10 μm. The averaged pore structure information obtained from all directions is quite close to that from one direction (parallel to bedding orientation). Therefore, we hypothesize that

the entire pore network is predominantly connected by spherical or elliptical pores, and there seems to be few closed pores across the nm- to μm-scales.

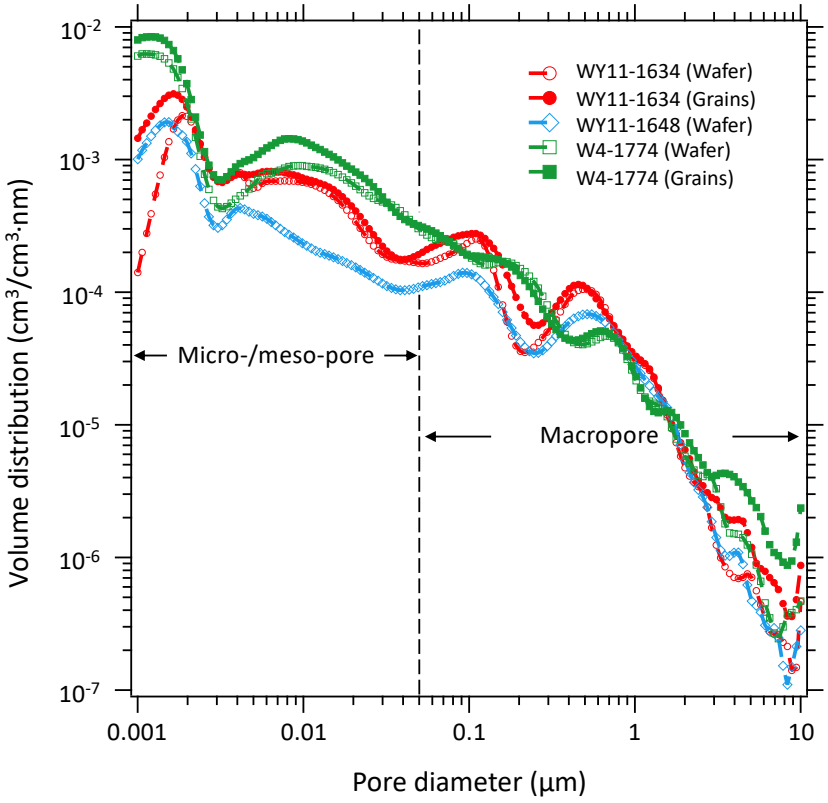

Figure 8. (U)SANS-generated pore size distribution (from PDSM analysis) in the detecting size range (1 nm to 10 μm) for tested samples.

Comparing porosity results obtained from MICP and (U)SANS (Tables 3 and 4), the former has an overall larger porosity than the latter probably due to its broader measuring size range (3 nm to 1 mm). (U)SANS provides a way to measure pore volumes of the micropores (< 2 nm), and it indicates that for these samples the contribution from micropores is almost negligible compared with that from meso/macropores, regardless whether it's more carbonate-rich or clay-

rich. A great portion of porosity, as measured by MICP, comes from large pores or microfractures larger than 10 μm (Figure 5), and this is verified by our observations of SEM images (Figure 4).

4. Conclusion

Two major organic-rich mudstone types, i.e., silica-rich carbonate and carbonate/siliceous mudstones, are identified in the Qianjiang E*q*3 unit oil groups, and characterized by high TOC content, porosity and permeability. Mineral pores are the primary pore types with a much higher percentage of intraparticle pores in the silica-rich carbonate mudstone, and a higher proportion of interparticle pores in the carbonate/siliceous mudstones. Organic matters are not widely distributed even with a modest TOC content, and organic matter-hosted pores are not visible as a result of low-medium OM maturation. Mineral-controlled pores in these two types of mudstones are dominant with various sizes ranging from μm-scale to nm-scale.

A combined MICP and (U)SANS analysis is capable of yielding specific pore information in a wide measurable size range. For silica-rich carbonate mudstones, macropores dominate the pore system with micropores (< 2 nm) and mesopores (2-50 nm) contributing no more than 20% of the total porosity, and over 80-90% of the pore volume is provided by pores interconnected by pore-throats in the range of 0.02-1 μm. For carbonate/siliceous mudstones, a higher proportion (> 25%) of micro/mesopores is most likely to be contributed by clay-related interparticle pores, and the pore volumes are mostly associated with pores that have a pore-throat size of 5-500 nm. In addition, it can also be concluded that the studied E*q*3 Qianjiang mudstones have few isolated pore spaces with a highly connected pore system under 1 μm.

In E*q*3 saline lacustrine shale samples, MICP approach detects more percentage of pores controlled by larger than 10 μm in pore-throat sizes. The well connected, large, dissolved, and intraparticle pores (>10 μm) in silica-rich carbonate mudstones or the micro-fractures in carbonate/siliceous mudstones can both create effective pathways for fluid migration, and therefore, explains the high permeability in these samples. The MICP results of two salt samples provide the evidence of a low-permeable seal for shale layers to indicate an overall good reservoir condition.

In summary, laboratory-based petrophysical analyses of the saline lacustrine shale samples, using integrated MICP, SANS/USANS, and FE-SEM approaches, indicates the presence of well-connected μm-nm-scale shale pore networks in the E*q*3 unit of the Qianjiang Formation and proves the excellent reservoir properties created by the cyclotherms of alternating salt and mudstone.

5. Acknowledgments

Financial supports from the Foundation of State Key Laboratory of Shale Oil and Gas Enrichment Mechanisms and Effective Development (No. G5800-16-ZS-KFZY006) at Petroleum Exploration and Production Research Institute of Sinopec, and the National Natural Science Foundation of China (Nos. 41830431 and 41672251) are greatly appreciated. Access to SANS NG7-30m and USANS BT5 was provided by the Center for High Resolution Neutron Scattering, a partnership between the National Institute of Standards and Technology and the National Science Foundation under Agreement No. DMR-1508249. Certain commercial equipment, instruments, or materials are identified in this paper to foster understanding. Such identification does not imply recommendation or endorsement by the National Institute of

Standards and Technology, nor does it imply that the materials or equipment identified are necessarily the best available for the purpose.

6. References

Anovitz, L. M., and D. R. Cole, 2015, Characterization and analysis of porosity and pore structures: Reviews in Mineralogy and Geochemistry, v. 80, p. 61-164, doi:10.2138/rmg.2015.80.04.

Bahadur, J., Y. B. Melnichenko, M. Mastalerz, A. Furmann, and C. R. Clarkson, 2014, Hierarchical pore morphology of Cretaceous shale: A small-angle neutron scattering and ultrasmall-angle neutron scattering study: Energy and Fuels, v. 28, no. 10, p. 6336-6344, doi:10.1021/ef501832k.

Bahadur, J., C. R. Medina, L. He, Y. B. Melnichenko, J. A. Rupp, T. P. Blach, and D. F. R. Mildner, 2016, Determination of closed porosity in rocks by small-angle neutron scattering: Journal of Applied Crystallography, v. 49, no. 6, p. 2021-2030, doi: 10.1107/S1600576716014904.

Bale, H. D., and P. W. Schmidt, 1984, Small-angle X-ray-scattering investigation of submicroscopic porosity with fractal properties: Physical Review Letters, v. 53, no. 6, p. 596.

Blach, T., A. P. Radlinski, D. S. Edwards, C. J. Boreham, C. Rehm, L. De Campo, and E. P. Gilbert, 2018, Fingerprint of hydrocarbon generation in the southern Georgina Basin, Australia, revealed by small angle neutron scattering: International Journal of Coal Geology, v. 186, p. 135-144.

Barker, J. G., C. J. Glinka, J. J. Moyer, M. H. Kim, A. R. Drews, and M. Agamalian, 2005,

Design and performance of a thermal-neutron double-crystal diffractometer for USANS at NIST: Journal of Applied Crystallography, v. 38, no. 6, p. 1004-1011, doi: 10.1107/S0021889805032103.

Chen, K. Y., B. J. Liu, Z. S. Shi, and J. Shi., 2002, Geochemistry character in Paleo- saline depositional sequence on Qianjiang group in Qianjiang depression: Journal of Salt Lake Research, v. 10, p. 19-24.

Chen, F. L., 2007, Structural evolution and depositional packing as well as hydrocarbon accumulation in Qianjiang Salt Lake Basin: Journal of Oil and Gas Technology v. 29, p. 50-53.

Clarkson, C. R., M. Freeman, L. He, M. Agamalian, Y. B. Melnichenko, M. Mastalerz, R. M. Bustin, A. P. Radliński, and T. P. Blach, 2012, Characterization of tight gas reservoir pore structure using USANS/SANS and gas adsorption analysis: Fuel, v. 95, p. 371–385, doi:10.1016/j.fuel.2011.12.010.

Fang, Z. X., K. Y. Chen, X. H. Yang, and C. J. Huang, 2003, Sequence stratigraphy characteristic of Qianjiang saline sub-basin: Journal of Salt Lake Research, v. 11, p. 14-23.

Gamero-Diaz, H., and C. Miller, 2012, sCore: A classification scheme for organic mudstones based on bulk mineralogy: AAPG Search and Discovery Article, No. 40951.

Gao, Z. Y., and Q. H. Hu, 2013, Estimating permeability using median pore-throat radius obtained from mercury intrusion porosimetry: Journal of Geophysics and Engineering, v. 10, no. 2, p. 025014.

Gao, Z. Y., and Q. H. Hu, 2015, Investigating the effect of median pore-throat diameter on spontaneous imbibition. Journal of Porous Media, v. 18, no. 12, p. 1231-1238, doi: 10.1615/JPorMedia.v18.i12.60.

Gao, Z. Y., Q. H. Hu, and H. Liang, 2013, Gas diffusivity in porous media: determination by mercury intrusion porosimetry and correlation to porosity and permeability: Journal of Porous Media, v. 16, no. 7, p. 607-617, doi:10.1615/JPorMedia.v16.i7.30.

Grice, K., S. Schouten, K. E. Peters, and J. S. S. Damsté, 1998, Molecular isotopic characterisation of hydrocarbon biomarkers in Palaeocene--Eocene evaporitic, lacustrine source rocks from the Jianghan Basin, China: Organic Geochemistry, v. 29, no. 5-7, p. 1745-1764, doi: 10.1016/S0146-6380(98)00075-8.

Gu, X., D. R. Cole, G. Rother, D. F. R. Mildner, and S. L. Brantley, 2015, Pores in Marcellus shale: A neutron scattering and FIB-SEM study: Energy and Fuels, v. 29, no. 3, p. 1295-1308, doi: 10.1021/acs.energyfuels.5b00033.

Guo, F. F., F. Zhang, W. Zhang, and W. X. Tang, 2012, Hydrocarbon accumulation rules of Wangchang Oilfiled in Qianjiang Sag: Lithologic Reservoirs, v. 5, p. 007 (in Chinese with English abstract).

Hall, P. L., D. F. R. Mildner, and R. L. Borst, 1986, Small-angle–scattering studies of the pore spaces of shaly rocks: Journal of Geophysical Research, v. 91, p. 2183-2192, doi:10.1029/JB091iB02p02183.

Hou, Y. G., F. R. Wang, S. He, T. Dong, and S. Q. Wu, 2017, Properties and shale oil potential of saline lacustrine shales in the Qianjiang Depression, Jianghan Basin, China: Marine and Petroleum Geology, v. 86, p.1173-1190, doi: 10.1016/j.marpetgeo.2017.07.008.

Hu, Q. H., Y. X. Zhang, X. H. Meng, Z. Li, Z. H. Xie, and M. W. Li, 2017, Characterization of multiple micro-nano pore networks in shale oil reservoirs of Paleogene Shahejie Formation in Dongying Sag of Bohai Bay Basin, East China: Petroleum Exploration and Development, v. 44, no. 5, p. 720-730.

Huang, C., and L. Hinnov, 2014, Evolution of an Eocene-Oligocene saline lake depositional system and its controlling factors, Jianghan Basin, China: Journal of Earth Science, v. 25, no. 6, p. 959-976.

Ilavsky, J., and P. R. Jemian, 2009, Irena: Tool suite for modeling and analysis of small-angle scattering: Journal of Applied Crystallography, v. 42, no. 2, p. 347–353, doi:10.1107/S0021889809002222.

Li Y. L., Q. Fang, Y. B. Ke, J. X. Dong, G. D. Yang, X. Ma, 2012, Effect of high salinity on CO_2 geological storages: A case study of Qianjiang Depression in Jianghan Basin: Journal of China Univerisity of Geosciences, Earth Sciences, v. 37, no. 2, p. 283-288 ().

Kline, S. R., 2006, Reduction and analysis of SANS and USANS data using IGOR Pro: Journal of Applied Crystallography, v. 39, no. 6, p. 895-900, doi: 10.1107/S0021889806035059.

Katz, A. J., and A. H. Thompson, 1986, Quantitative prediction of permeability in porous rock: Physical Review B, v. 34, no. 11, p. 8179-8181.

Katz, A. J., and A. H. Thompson, 1987, Prediction of rock electrical conductivity from Mercury injection measurements: Journal of Geophysical Research: Solid Earth, v. 92, p. 599-607.

King, H. E., A. P. R. Eberle, C. C. Walters, C. E. Kliewer, D. Ertas, and C. Huynh, 2015, Pore architecture and connectivity in gas shale: Energy and Fuels, v. 29, no. 3, p. 1375-1390, doi: 10.1021/ef502402e.

Kline, S. R., 2006, Reduction and analysis of SANS and USANS data using IGOR Pro: Journal of Applied Crystallography, v. 39, no. 6, p. 895-900, doi:10.1107/S0021889806035059.

Lake, J. A., 1967, An iterative method of slit-correcting small angle X-ray data: Acta Crystallographica, v. 23, no. 2, p. 191-194, doi: 10.1107/S0365110X67002440.

Li, M. W., Z. H. Chen, T. T. Cao, X. X. Mac, X. J. Liu, Z. M. Li, Q. G. Jiang, and S. Q. Wu.

2018, Expelled oils and their impacts on Rock-Eval data interpretation, Eocene Qianjiang Formation in Jianghan Basin, China. Intern. J. Coal Geol., 191: 37-48.

Liu, M., Z. Y. Chen, K. Li, 2010, The source and migration direction of the high maturity oil of the Eq4 in Wangchang structure, North of Qianjiang: Jianghan Petroleum Science and Technology, v. 20, p. 1-4 (in Chinese with English abstract).

Mastalerz, M., L. He, Y. B. Melnichenko, and J. A. Rupp, 2012, Porosity of coal and shale: Insights from gas adsorption and SANS/USANS techniques: Energy and Fuels, v. 26, no. 8, p. 5109–5120, doi:10.1021/ef300735t.

Melnichenko, Y., 2016, Small-angle scattering from confined and interfacial fluids: Applications to energy storage and environmental science: Springer, 314 p, doi: 10.1007/978-3-319-01104-2.

Peters, K. E., A. E. Cunningham, C. C. Walters, J. G. Jiang, and Z. A. Fan, 1996, Petroleum systems in the Jiangling-Dangyang area, Jianghan basin, China: Organic Geochemistry, v. 24, no. 10-11, p. 1035-1060.

Philp, R. P., L. Jinggui, and C. A. Lewis, 1989, An organic geochemical investigation of crude oils from Shanganning, Jianghan, Chaidamu and Zhungeer Basins, People's Republic of China: Organic Geochemistry, v. 14, no. 4, p. 447-460.

Radlinski, A. P., E. Z. Radlinska, M. Agamalian, G. D. Wignall, P. Lindner, and O. G. Randl, 1999, Fractal Geometry of Rocks: Physical Review Letters, v. 82, p. 3078–3081, doi:10.1103/PhysRevLett.82.3078.

Radlinski, A. P., C. J. Boreham, P. Lindner, O. Randl, G. D. Wignall, A. Hinde, and J. M. Hope, 2000, Small angle neutron scattering signature of oil generation in artificially and naturally matured hydrocarbon source rocks: Organic Geochemistry, v. 31, no. 1, p. 1-14, doi:

10.1016/S0146-6380(99)00128-X.

Radlinski, A.P., M. Mastalerz, A. L. Hinde, M. Hainbuchner, H. Rauch, M. Baron, J. S. Lin, L. Fan, and P. Thiyagarajan, 2004, Application of SAXS and SANS in evaluation of porosity, pore size distribution and surface area of coal: International Journal of Coal Geology, v. 59, no. 3, p. 245-271, doi:10.1016/j.coal.2004.03.002.

Ruppert, L. F., R. Sakurovs, T. P. Blach, L. He, Y. B. Melnichenko, D. F. R. Mildner, and L. Alcantar-Lopez, 2013, A USANS/SANS study of the accessibility of pores in the Barnett shale to methane and water: Energy and Fuels, v. 27, no. 2, p. 772-779, doi: 10.1021/ef301859s.

Sakurovs, R., L. Koval, M. Grigore, A. Sokolova, L. F. Ruppert, and Y. B. Melnichenko, 2017, Nanometre-sized pores in coal: Variations between coal basins and coal origin: International Journal of Coal Geology, v. 186, p. 126–134, doi:10.1016/j.coal.2017.11.010.

Sun, M. D., B. S. Yu, Q. H. Hu**,** R. Yang, Y. F. Zhang, B. Li, Y. B. Melnichenko, and G. Cheng, 2018, Pore structure characterization of organic-rich Niutitang Shale in China: Small Angle Neutron Scattering (SANS) study: *International Journal of Coal Geology*, v. 186, p. 115-125.

Ulmishek, G. F., 1992, Geology and hydrocarbon resources of onshore basins in eastern Chin: US Geological Survey, no. 93-4.

Wang, G. L., Y. Q. Yang, Y. S. Zhang, Z. X. Qi, Y. D. Qiao, and H. R. Yuan, 2004, Sedimentarymicrofacies and evolution of the Qianjiang Formation of Paleogene Wangchang area in Qianjiang Sag, Jianghan Basin: Journal of Palaeogeography, v. 6, p. 140-150.

Wang, G. L., Y. S. Zhang, and Y. Q. Yang, 2004b, Evaluation of non-sandstone reservoirs

between salt beds of the Paleogene Qianjiang Formation in the Qianjiang depression of Jianghai Basin. Petroleum Geology & Experiment, v. 26, p. 462-468.

Wang, K., J. R. Ye, F. F. Guo, X. C. Li, J. M. Chen, 2011, Characteristics and hydrocarbon generation-expulsion history of source rock of Banghu syncline in Qianjiang depression: Geological Science and Technology Information, v. 30, p. 83-88.

Wang, S., F. Javadpour, and Q. Feng, 2016, Confinement correction to mercury intrusion capillary pressure of shale nanopores: Scientific Reports, v. 6, p. 20160, doi: 10.1038/srep20160.

Washburn, E. W, 1921, The dynamics of capillary flow: Physical review, v. 17, no. 3, p. 273-283, doi: 10.1103/PhysRev.17.273.

Webb, P. A, 2001, An Introduction To The Physical Characterization of Materials by Mercury Intrusion Porosimetry with Emphasis On Reduction And Presentation of Experimental Data. Micromeritics Instrument Corp, Norcross, Georgia.

Wu, S., X. Tang, X. Du, W. Liang, Q. He, 2013, Geologic characteristics of continental shale oil in the Qianjiang depression, Jianghan Salt Lake Basin: Journal of East China Institute of Technology, v. 36, no. 3, p. 282-286 (in Chinese with English abstract).

Yang, R., S. He, Q. H. Hu, M. D. Sun, D. F. Hu, and J. Z. Ye, 2017, Applying SANS technique to characterize nano-scale pore structure of Longmaxi shale, Sichuan Basin (China): Fuel, v. 197, p. 91-99.

Zhao, J. H., Z. J. Jin, Q. H. Hu, Z. K. Jin, T. J. Barber, Y. X. Zhang, and M. K. Bleuel, 2017, Integrating SANS and fluid-invasion methods to characterize pore structure of typical American shale oil reservoirs: Scientific Reports, v. 7, p. 15413. doi: 10.1038/s41598-017-15362-0

Zheng, Y. H., 2010, Exploration direction and strategy for lithologic accumulations in Qianjiang Formation of the Qianjiang sag, Jianghan Basin: Petroleum Geology & Experiment, v. 4, p. 007 (in Chinese with English abstract).

Chapter 4: Multiscale Quantification of Shale Wettability

Yuxiang Zhang[1], Troy J. Barber[1], Qinhong Hu[1, *], and Markus Bleuel[2,3]

[1]Department of Earth and Environmental Sciences, University of Texas at Arlington, Arlington, Texas, USA.

[2]Center for Neutron Research, National Institute of Standards and Technology, Gaithersburg, Maryland, USA.

[3]Department of Materials Science and Engineering, University of Maryland College Park, Maryland, USA.

Key Points

Multiscale pore structure and wettability of shale are characterized by small angle neutron scattering approach with a contrast matching technique

Submitted to:

Geophysical Research Letters

*Corresponding author: Qinhong Hu (maxhu@uta.edu)

Abstract

Multiscale pore structure characterization is of critical importance to understand hydrocarbon storage and transport in low-porosity/extra-low-permeability shale reservoirs. To investigate the pore structure, the combined (ultra-) small angle neutron scattering measurements, (U)SANS, was employed to quantify the porosity and characterize pore size distribution at nm-μm scales (pore diameter: 1 nm - 10 μm). Furthermore, a contrast matching technique was adopted in (U)SANS approaches to differentiate accessible (open) pores and inaccessible (closed) pores as a function of pore size, with respect to oil- and water-accessible pores. Working with two Utica and two Bakken shale samples with different total organic carbon contents, maturation, and mineralogy, our results show that around 40-70% of the pores in studied Utica shales are accessible to oil and around 34-37% of the pores are water wet. In contrast, the studied Bakken shales are not preferentially wet by oil or water, with less than 36% of the pores accessible to both fluids.

1. Introduction

The investigation of multiscale pore structure of shales is essential to understand wettability, fluid flow, and ultimate recovery in unconventional reservoirs. In the past two decades, small angle neutron scattering (SANS) and ultra-small angle neutron scattering (USANS) techniques have been increasingly and successfully employed for characterizing pore structure of complex geological samples (e.g., coals, sandstones, carbonates, shales), as reported in many literature (e.g., Radlinski et al., 1999; Radlinski et al., 2004; Clarkson et al., 2012; Melnichenko et al., 2012; Anovitz and Cole, 2015; Gu et al., 2016; Zhao et al., 2017; Zhang et al., 2018). Compared with fluid intrusion and gas physisorption techniques, e.g., mercury intrusion capillary pressure (MICP) analysis and low-pressure gas sorption isotherm, the combined SANS/USANS approach takes advantage of measuring total porosity (including closed porosity not-accessible to fluid techniques), pore size distribution (PSD), and specific surface area (SSA), over a broad pore length (diameter) spectrum from ~1 nm to ~20 μm (Radlinski et al., 2004; Anovitz and Cole, 2015).

In addition to the full-spectrum measurement of PSD, Melnichenko et al. (2012) proposed that the "contrast matching" approach could be used in SANS/USANS studies to quantify accessible vs. inaccessible porosity by immersing the porous solids with "contrast matching" fluids. These contrast matching fluids can be isotopic mixtures of solvents (e.g., H_2O+D_2O) or pressurized deuterated methane (CD_4) which aim to match the neutron scattering length density (SLD) of the solid matrix and therefore, the neutron scattering only comes from inaccessible pores (Melnichenko et al., 2012). Since then, this technique has been widely employed by geologists to study accessible vs. inaccessible porosity in coal and shale samples (e.g., Mastalerz et al., 2012;

Clarkson et al., 2013; Sakurovs et al., 2017; Liu et al., 2019), or organic porosity and water-accessible porosity in shales (Gu et al., 2015; 2016).

However, it is worthy of mentioning two limitations of these previous studies. First, when using pressurized CD_4 as the contrast agent, the "zero contrast" point may be ambiguous when it comes to high neutron SLD matrix (e.g., restricted by the in situ pressure of the pressure cell). Second, when using isotopic mixtures (e.g., D_2O+H_2O), the wettability of the matrix compositions (especially the organic matter) greatly impacts the saturation of isotopic mixtures in the pore networks. As a result, the closed porosity may be overestimated because not all accessible (open) pores are immersed by contrast matching fluids. Therefore, in this work, instead of only referring to the measurement of accessible/inaccessible porosity, we used both n-decane (an oil-phase fluid) and water to quantify and compare the volume fraction of oil-accessible and water-accessible pores at different scales. Working with two leading shales in the United States with different total organic carbon (TOC) contents, maturity, and mineralogy, this study's primary goals are to (1) measure the total porosity and characterize the pore size distribution of shale samples over a wide size range of 1 nm to 10 μm in diameters; and (2) quantify oil- and water-accessible porosities over the same length scale and characterize the wetting behavior at different scales.

2. Materials and Methods

2.1 Sample selection and preparation

Four core samples of the Utica and the Bakken Shale were acquired and used for this study. Detailed sample information is given in Table 1. The first Utica sample (depth: 1149 ft; TOC: 7.22 wt.%) is in the early oil window and the second Utica sample (depth: 5685 ft; TOC: 3.60

wt.%) has a higher maturity in the oil-gas window. Two Bakken samples are collected from the upper and lower Bakken members, respectively, and are both in the oil window. All four samples have a relatively close weight fraction of clay minerals (13.8-25.3 wt.%). The main difference lies in the other minerals, where carbonates (mostly calcite and dolomite) are the most substantial fraction in the Utica samples (43.2-60.3 wt.%) while Bakken samples show a more significant fraction of quartz and feldspar (36.1-59.9 wt.%). In addition, compared with the Utica samples (TOC: 3.60-7.22 wt.%), organic matters (kerogen or bitumen) are much more abundant in the Bakken samples (TOC: 13.7-21.6 wt.%). Therefore, the investigation and comparison of multiscale pore structure in these two shales will have profound importance to the geological controls to guide future studies of other unconventional reservoir rocks.

Table 1. The formation, location, depth, bulk mineralogy, and TOC of the selected samples

Sample	Shale	Depth	Bulk mineralogy (wt.%)*				TOC
		(ft)	QF	Carb.	Clay	Others	(wt.%)
Utica 1	Utica	1149	19.78	43.15	24.49	12.58	7.22
Utica 2	Utica	5685	14.37	60.33	18.70	6.60	3.60
Bakken 1	Bakken (upper member)	10064	59.90	9.00	25.30	5.80	13.65
Bakken 2	Bakken (lower member)	10124	36.10	29.20	13.80	20.90	21.64

Q: quartz; F: feldspar; Carb: carbonates

Previous SANS/USANS studies on shales mostly used thin sections (150-200 μm thick) or wafers (around 500 μm thick) to characterize pore geometry either parallel or perpendicular to the shale lamination (Gu et al., 2015; Sun et al., 2017; Zhao et al., 2017; Blach et al., 2018). In this study, we used crushed rock particles (hand ground with a mortar and pestle) for obtaining

an averaged pore structure information from all orientations, and the grains were sieved to a particle size of 177-500 μm (35/80 mesh) (Figure 1a) which is consistent with the grain size we use in other tests (e.g., MICP, N_2 physisorption). The resulting samples were then oven-dried at 60°C to a constant weight (at least 24 hours) to remove moistures in the open pore networks before use. Afterward, these dry sample particles were loaded into a pre-assembled titanium cell from the top hole and sealed prior to performing (U)SANS analyses (Figure 1b). For each sample, we prepared a set of cells, one cell for dry sample test, and three cells for contrast matching ones to determine the best neutron SLD (see section 2.2).

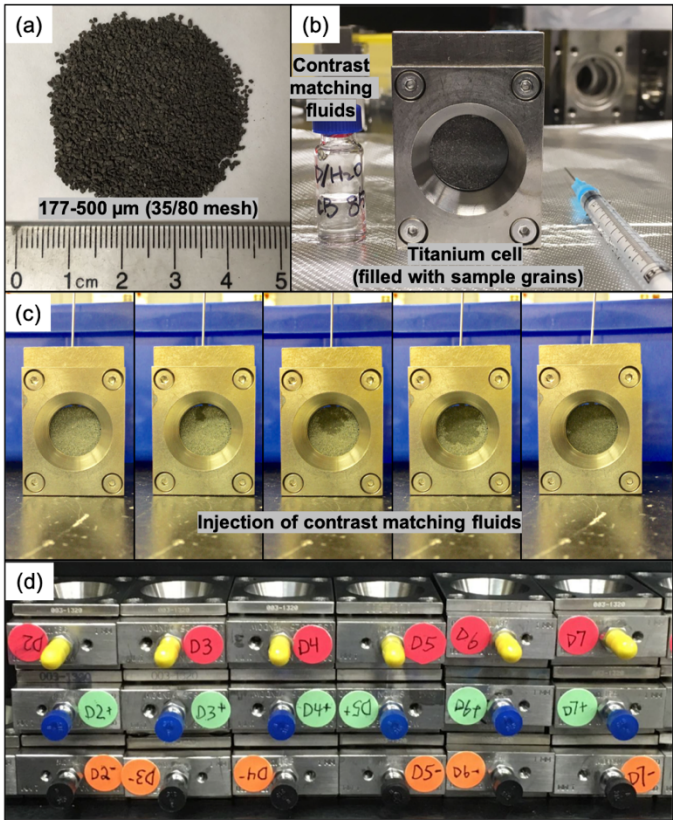

Figure 1. (a) Granular samples with a particle size of 177-500 μm; (b) Prepared contrast matching fluid (left), titanium cell filled up with sample grains, and syringe used for injecting fluids (right); (c) Fluid

injection process from less fluid saturation (left) to complete fluid saturation (right); (d) Prepared contrast matched samples (with SLD-, SLD, SLD+ values)

2.2 Contrast matching fluids

The calculation of average neutron SLD is important before the preparation of contrast matching fluids. Shale rocks are heterogeneous, as such, material properties such as the neutron SLD value fluctuates throughout the specimen volume. The SLD of each sample's rock matrix, or ρ_{matrix}, is computed from rock's composition (Radlinski and Boreham, 1996) according to the equation, $\rho_{matrix} = \sum_{i=1}^{n} \phi_i \rho_i$, where ϕ_i and ρ_i are the volume concentration and neutron SLD of each mineral component (including organic matter).

To produce the contrast matching fluids that have the SLD values same or close to the rock matrix, we prepared four solvents: (1) water (H_2O); (2) deuterated water (D_2O); (3) n-decane ($C_{10}H_{22}$); and (4) deuterated n-decane ($C_{10}D_{22}$). The mass density and neutron scattering length density of these solvents are listed in Table 2. The mole ratio of deuterated solvent and protonated solvent (e.g., D_2O/H_2O) is determined using the SLD calculator (https://sld-calculator.appspot.com/) and then converted into mass ratio.

Table 2. Mass density at room temperature and neutron scattering length density of four solvents

	Mass density (g/cm^3)	Scattering length density (10^{-6} cm^{-2})
H_2O	1	-0.56
D_2O	1.11	6.39
$C_{10}H_{22}$	0.73	-0.49
$C_{10}D_{22}$	0.84	6.56

However, the computed average neutron SLD may not perfectly match the rock matrix because very small-scale heterogeneity of shales inherently leads to difficulties and uncertainties in measuring its composition during the XRD and TOC tests. Therefore, we employed an empirical approach to dealing with this uncertainty by choosing upper (+10%) and lower (-10%) bounds of the computed neutron SLD and will refer these bounds throughout the remainder of the paper as "SLD+" and "SLD-" values, respectively. Then, for each sample, we calculated the mass ratio of $C_{10}D_{22}/C_{10}H_{22}$ using the values of SLD+ and SLD-. According to the mass ratio, we prepared three sets of contrast matching solvents (isotopic mixtures of n-decane) and used a syringe to inject the solvents into three cells which were loaded with the same dry sample grains (Figure 1b-c). After the grains were fully saturated with the solvents, we sealed the cells and labeled them with symbols '+', '=' at a target SLD, and '-', representing three SLD values (Figure 1d).

2.3 SANS/USANS measurement and data collection

Small angle neutron scattering measurement was performed on the NG7-30m SANS instrument at NIST Center for Neutron Research (NCNR), using three sample-to-detector distances (1.0, 4.0, and 15.3 m). The wavelength λ used for these three distances is 6.0 Å. The scattering intensity, I(Q), was measured as a function of scattering vector Q, which is expressed as $Q = 4\pi\lambda^{-1}\sin\theta$, where λ is the wavelength of the neutron beam and 2θ is the scattering angle (Melnichenko, 2016). The collected SANS 2-D scattering patterns (from each detector geometry) were processed by Igor Pro for data correction and then normalized relative to open beam intensity and radially averaged 1-D scattering profile (Kline, 2006). The 1-D scattering profile at

three distances was afterward merged together with a resultant coverage of Q-range at ~0.001 $Å^{-1}$ - ~0.5 $Å^{-1}$.

Ultra-small angle neutron scattering was conducted on the BT-5 USANS instrument at NCNR with a mean wavelength of λ=2.38 Å (range 2.31-2.45 Å), covering a scattering vector Q range from ~3×10^{-5} to ~0.006 $Å^{-1}$ (Barker et al., 2005). Using the NCNR USANS reduction macros (Kline, 2006), the collected USANS data was first reduced with an empty beam background and converted to an absolute scale and then processed for desmearing (Blach et al., 2017). Lastly, the desmeared USANS profile was combined with the 1-D SANS data to obtain a broad Q range of ~2.5×10^{-5} $Å^{-1}$ to ~0.5 $Å^{-1}$.

In the experiment, SANS and USANS measurements were first conducted on all four dry samples to obtain the full spectrum of PSD. Secondly, we performed a quick SANS measurement at the sample-to-detector distance of 1 meter on three sets of contrast-matched samples. These are samples immersed by isotopic mixtures of n-decane ($C_{10}D_{22}$+$C_{10}H_{22}$) with three specific values (SLD+, SLD, SLD-). It is not difficult to find the one which has the lowest scattering intensity from 1-D scattering curves in the medium-high-Q range (~0.03 - ~0.1 $Å^{-1}$) and this sample is named as the “best contrast-matched” sample. The neutron SLD value for this “best contrast-matched” sample would be the closest one to the shale matrix and be further named as the “best average neutron SLD”. All four shale samples were measured through the same procedure until the best average neutron SLD value for each one was. Then, we performed a complete SANS and USANS measurements over the full-Q range on the selected best contrast-matched samples. Lastly, we made the isotopic mixtures of water (D_2O+H_2O) according to the best average neutron SLD value of each sample and measured the samples contrasted by these solvents.

3. Data analysis

The combined SANS/USANS datasets were loaded into the Igor Pro *Irena macro* (Ilavsky and Jemian, 2009) and analyzed by the size distribution tool (method: IPG/TNNLS) using a "spheroid" shape model with no data errors. The selected Q-range for modeling is from 5×10^{-5} $Å^{-1}$ to 0.3 $Å^{-1}$, which corresponds to an approximate pore diameter of 1 nm to 10 μm, according to the relation $r\approx2.5/Q$ (Radlinski, 2000). The "best average neutron SLD" is used in the model for each sample. Through the "Evaluate Size Distributions" function in Irena macro, the cumulative PSD could be directly generated. The porosity in the measurable size range, as well as incremental porosity as a function of pore size, were consequently derived.

4. Results and Discussion

4.1 The best average neutron SLD

The specific mineralogical composition and TOC content were determined through X-ray diffraction (XRD) and TOC tests, respectively. All compositions present in the selected four samples are given with their neutron SLDs (Figure 2), which could also be calculated based on the chemical composition in the SLD calculator. In addition, the calculated average SLD of each sample, as well as the upper (+10%) and lower (-10%) bounds, is also shown in Figure 2.

Table 3 exhibits the calculated average neutron SLD of the shale matrix, together with three SLD values set for isotopic mixtures of n-decane ($C_{10}D_{22}$+ $C_{10}H_{22}$). The best average neutron SLD was marked with an asterisk and the corresponding mole ratio, and the mass ratio of D/H for isotopic solvents are listed.

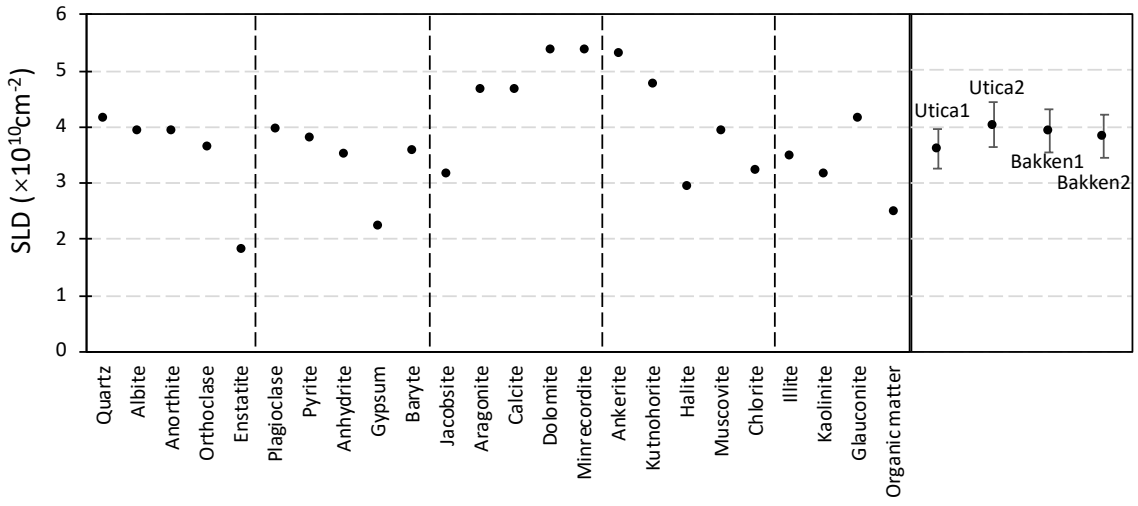

Figure 2. SLD values of compositions presented in four shale samples and calculated average neutron SLDs for each sample; the neutron SLD of organic matters can be variable, and we select an average value of $2.5\times10^{10}cm^{-2}$.

Table 3. Neutron SLD of shale matrix and solvents (with three different values) for each sample.

Sample ID	SLD	SLD-	SLD	SLD+	D/H molar ratio	D/H mass ratio	D/H molar ratio	D/H mass ratio
	(matrix)	(solvent)			(n-decane)		(water)	
Utica 1	3.61	3.25	3.61	3.97*	63:37	1.97	65:35	2.07
Utica 2	4.04	3.64	4.04	4.44*	70:30	2.70	72:28	2.86
Bakken 1	3.93	3.53	3.93*	4.32	63:37	1.97	65:35	2.07
Bakken 2	3.82	3.43	3.82*	4.20	61:39	1.81	63:37	1.89

*The best average neutron SLD

4.2 Characteristics of SANS/USANS results

Take the first Utica shale for example, the combined SANS and USANS scattering profiles for the dry sample and its corresponding two contrast-matched samples are plotted together (Figure 3) and exhibit the following features:

(1) The scattering intensity I(Q) decreases after contrast matching fluids saturation in the low-Q region ($Q < 3\times10^{-4}$ $Å^{-1}$)

(2) Multiple scattering (where the scattering curve flattens out at very low-Q region) (Sabine and Bertram, 1999; Radliński et al., 1999) of the dry sample disappears after being contrast matched.

(3) Power-law scattering (i.e., the linear portion of the scattering curve) exists in the low-to-medium-Q region before and after contrast matching.

For the 1st feature, changes in scattering intensities are more evident in Utica samples than Bakken ones indicating that Utica samples are more fluid-accessible (both n-decane and water) in the large pore scale as more pores are contrast-matched by intruded solvents. The disappearance of multiple scattering (2nd feature) also reflects the effects of contrast matching. Previous SANS/USANS studies on rocks illustrated the power-law scattering (a linear relation in the low-to-medium Q) as a result of fractal pore geometry (e.g., Radlinski et al., 1999) at nm-μm scales and through 3rd feature we can conclude that the remaining pores (pores not invaded by solvents) still own the fractal properties.

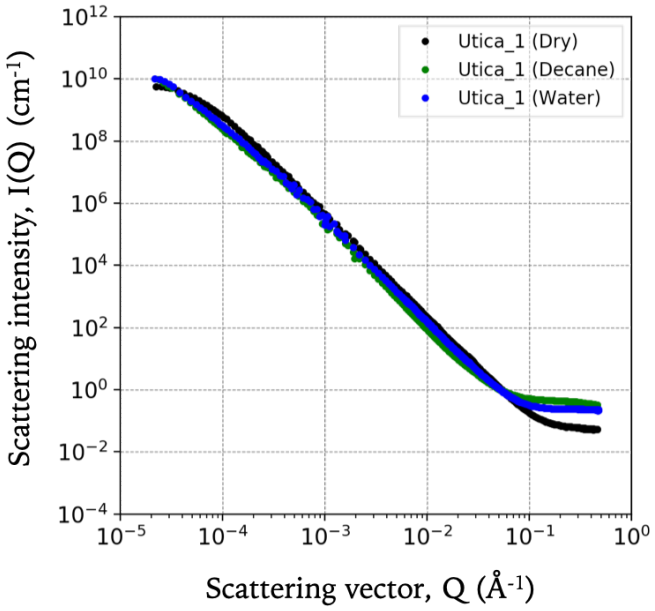

Figure 3. Combined SANS and USANS absolute scattering intensities plotted as a function of scattering vector Q (without error bars) using Utica_1 as an example. For comparison, the scattering profile of dry sample and contrast-matched samples (by n-decane and water) are plotted together.

4.3 Porosity and pore size distribution

When applying the contrast matching technique in (U)SANS measurements, the theoretical condition is that all open pores, which are connected to the surface of rock samples, are saturated with contrast-matching fluids which have the same (or close) neutron SLD ($\rho_{solvent}$) value to the surrounding matrix (ρ_{matrix}). In this situation, only inaccessible (closed) pores are measured in SANS/USANS experiments. However, realistically, "zero contrast" cannot be easily achieved because not only shale matrix has multiple components at μm-scale with inconsistent SLD values but also distinct wettability of minerals to different wetting fluids leads to an incomplete fluid saturation in pore networks.

Therefore, when dry sample grains are saturated with mixed solvents, all isolated (inaccessible) pores, as well as open pores which are not wetted by solvents, will be detected in

(U)SANS measurements. Based on this understanding, we are able to quantify the volume fraction of oil-accessible (loosely called hydrophobic) pores and water-accessible (hydrophilic) pores by simply using the difference of results in dry samples and contrast matched samples.

The results of total porosity, oil-accessible porosity, and water-accessible porosity for each sample are summarized in Figure 4. The generated pore size distributions from *Irena macro* are illustrated in Figure 5 as the incremental porosity vs. pore diameter. The size distribution of dry samples can be directly generated from the scattering profile of dry samples. However, to obtain size distributions of oil-accessible/water-accessible pores, we need to first generate the PSD of contrast-matched samples, which incorporate isolated pores and non-wetting pores, and then subtract it from the PSD of dry samples.

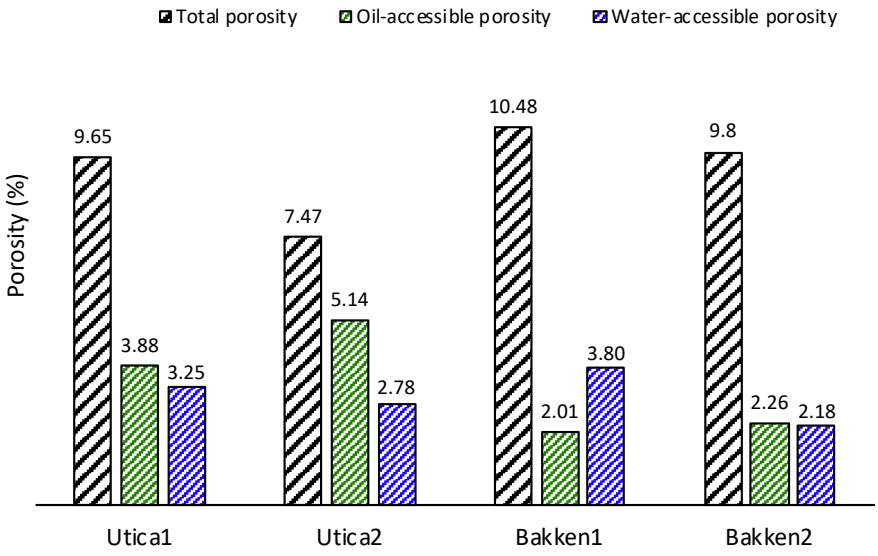

Figure 4. Histogram of SANS/USANS measured total porosity for each sample (marked in black), and derived oil-accessible porosity (green) and water-accessible porosity (blue).

Figure 4 shows that, for each sample, the measured total porosity (7.47-10.5%), is larger than oil-accessible/water-accessible porosity (2.01-5.14%). The difference comes from the porosity of closed pores and the pores which are not occupied by fluids. In Utica shale samples, the volume of oil-accessible pores is larger than water-accessible ones (Figure 5), which indicates that Utica samples are more oil -wettable. In comparison, two Bakken shale samples are not preferentially wet by either oil or water, as there is not a significant difference between the size distribution of oil- and water-accessible pores (Figure 5). The variation in wettability among these samples seems to correlate with the proportion of minerals or organic matters.

Overall, we can see that the Utica Shales have a lower closed porosity and higher connectivity than the Bakken Shales as the proportion of accessible pores, either oil-accessible or water-accessible, is larger in two Utica samples (oil-accessible pores: 40.2-68.8%; water-accessible pores: 33.7-37.7%) than two Bakken samples (19.2-23.1% and 22.2-36.3%). It is noteworthy to mention that oil-accessible pores are not present in pores smaller than 3 nm, as indicated from PSD at pore diameter smaller than 3 nm (Figure 5), which may be related to the wettability at nanoscales or more probably the molecular size of n-decane (at 1.30×0.235× 0.178 nm to be too large to enter).

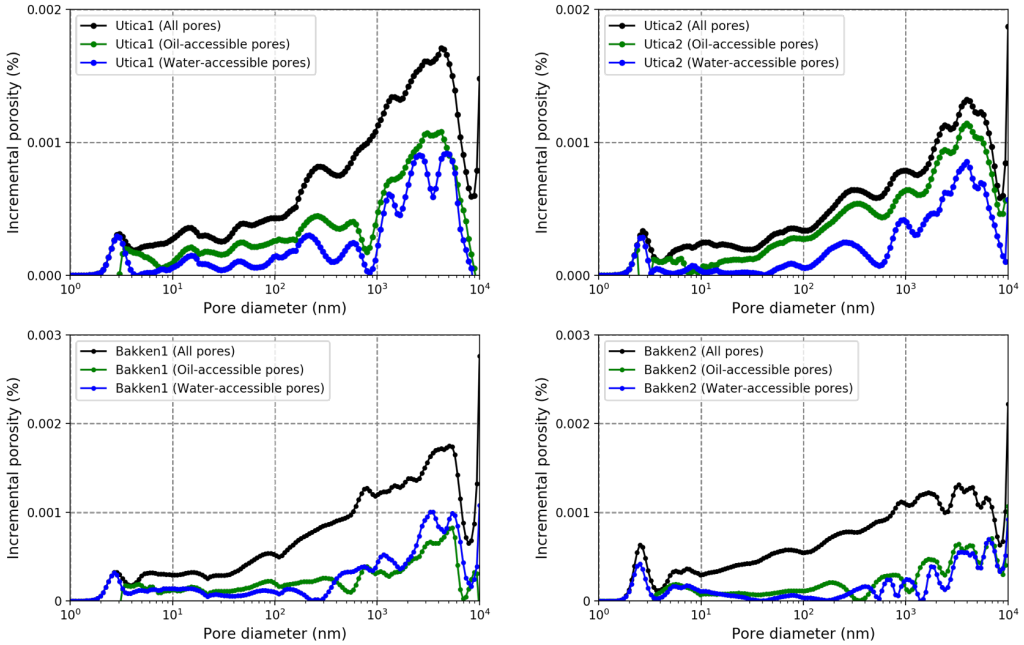

Figure 5. Size distributions of all pores, oil-accessible pores, and water-accessible pores, plotted as incremental porosity versus pore diameter.

4.4 Advantages and limitations of the new approach

In general, the application of contrast matching in combined SANS and USANS measurements has its unique advantages. It can be effectively used to quantify real total porosity, as well as fluid-accessible porosity which allows the comparison and observation of wettability at nm-μm scales. In addition, compared with low-pressure gas physisorption (N_2 or CO_2) or imaging techniques (SEM), the combined SANS/USANS approach has a much broader measuring size range (~1 nm - 10 μm) which give more pore structure information.

Some discussion of the limitations of this methodology is warranted. First of all, the data analysis was based on an assumption that all pores are of spherical shapes. Realistically, the pore type and shape of shales are very complicated, and there may be a significant portion of

cylindrical or slit-shaped pores. In a word, the derived porosity and PSD are based on the equivalent spherical diameters. Secondly, the juxtaposed distribution of minerals and organic matters leads to a variable presence of neutron SLD across the sample, and the contrast matching fluid prepared based on the average neutron SLD can only lower down the contrast between pores and solid grains, but it can never achieve a "zero contrast" everywhere in the shale matrix. Thirdly, the applied wetting fluids, n-decane, and water, have different molecular sizes. This may lead to a complicated interpretation of the wettability at pore scales smaller than 5 nm, as the absence of n-decane in this pore-size range (Figure 5) may be the molecular size effect.

5. Conclusions

Overall, this study showcases a new technique of applying contrast matching method in combined SANS and USANS measurements for Utica and Bakken shale samples with characteristic multiscale pore structure and mixed wettability. The innovative points lie in comparing the fluid-accessible porosity with total porosity, as well as applying different wetting fluids for investigating wettability from μm-scale down to nm-scale. Besides, the employment of granular samples (177-500 μm) allows fluids to sufficiently intrude pore networks for contrast matching which gives reliable measurements. Also, the selection of the best contrast matching fluids minimizes the influence of average neutron SLD on calculation in the modeling. Our overall results showed that around 40-70% of the pores in studied Utica Shales are oil-accessible and around 34-37% pores are water-accessible, while and the studied Bakken Shales are not preferentially wet by either oil or water with less than 23% of the oil-accessible pores and 22-36% of the water-accessible pores.

6. Acknowledgement

We acknowledge the funding support from AAPG Foundation's Grants-in-Aid Program, National Science Foundation Graduate Research Fellowship, and the Nuclear Energy University Program, Office of Nuclear Energy, U.S. Department of Energy (award number DE-NE0008797). Access to SANS NG7-30 and USANS BT5 instruments was provided by the Center for High Resolution Neutron Scattering, a partnership between the National Institute of Standards and Technology and the National Science Foundation under agreement No. DMR-1508249. We also thank Tomasz Blach and Katherine Gioseffi for their help during the SANS and USANS experiments.

6. References

Anovitz, L. M., & Cole, D. R. (2015). Characterization and analysis of porosity and pore structures. In *Reviews in Mineralogy and Geochemistry* (Vol. 80, pp. 61–164). https://doi.org/10.2138/rmg.2015.80.04

Bahadur, J., Medina, C. R., He, L., Melnichenko, Y. B., Rupp, J. A., Blach, T. P., & Mildner, D. F. R. (2016). Determination of closed porosity in rocks by small-angle neutron scattering. *Journal of Applied Crystallography*, *49*(6), 2021–2030. https://doi.org/10.1107/S1600576716014904

Bahadur, J., Ruppert, L. F., Pipich, V., Sakurovs, R., & Melnichenko, Y. B. (2018). Porosity of the Marcellus Shale: A contrast matching small-angle neutron scattering study. *International Journal of Coal Geology*, *188*(January), 156–164. https://doi.org/10.1016/j.coal.2018.02.002

Clarkson, C. R., Solano, N., Bustin, R. M., Bustin, A. M. M., Chalmers, G. R. L., He, L. (2013). Pore structure characterization of North American shale gas reservoirs using USANS/SANS,

gas adsorption, and mercury intrusion. *Fuel*, *103*, 606–616. https://doi.org/10.1016/j.fuel.2012.06.119

Gu, X., Cole, D. R., Rother, G., Mildner, D. F. R., & Brantley, S. L. (2015). Pores in Marcellus Shale: A neutron scattering and FIB-SEM study. *Energy and Fuels*, *29*(3), 1295–1308. https://doi.org/10.1021/acs.energyfuels.5b00033

Gu, X., Mildner, D. F. R., Cole, D. R., Rother, G., Slingerland, R., & Brantley, S. L. (2016). Quantification of Organic Porosity and Water Accessibility in Marcellus Shale Using Neutron Scattering. *Energy and Fuels*, *30*(6), 4438–4449. https://doi.org/10.1021/acs.energyfuels.5b02878

King, H. E., Eberle, A. P. R., Walters, C. C., Kliewer, C. E., Ertas, D., & Huynh, C. (2015). Pore architecture and connectivity in gas shale. *Energy and Fuels*, *29*(3), 1375–1390. https://doi.org/10.1021/ef502402e

Mastalerz, M., He, L., Melnichenko, Y. B., & Rupp, J. A. (2012). Porosity of coal and shale: Insights from gas adsorption and SANS/USANS techniques. *Energy and Fuels*, *26*(8), 5109–5120. https://doi.org/10.1021/ef300735t

Melnichenko, Y. B. (2016). *Small-angle Scattering from Confined and Interfacial Fluids*. Springer. https://doi.org/10.1007/978-3-319-01104-2

Melnichenko, Y. B., He, L., Sakurovs, R., Kholodenko, A. L., Blach, T., Mastalerz, M. (2012). Accessibility of pores in coal to methane and carbon dioxide. *Fuel*, *91*(1), 200–208. https://doi.org/10.1016/j.fuel.2011.06.026

Radliński, A. P., & Boreham, C. J. (1996). Microstructural evolution of source rocks during hydrocarbon generation: A small-angle-scattering study. *Physical Review*, *53*, 152–160.

Radliński, A. P., Radlińska, E. Z., Agamalian, M., Wignall, G. D., Lindner, P., & Randl, O. G. (1999). Fractal geometry of rocks. *Physical Review Letters*, 82(15), 3078–3081. https://doi.org/10.1103/PhysRevLett.82.3078

Radlinski, A. P. (2006). Small-Angle Neutron Scattering and the Microstructure of Rocks. *Reviews in Mineralogy and Geochemistry*, *63*(1), 363–397. https://doi.org/10.2138/rmg.2006.63.14

Ruppert, L. F., Sakurovs, R., Blach, T. P., He, L., Melnichenko, Y. B., Mildner, D. F. R., & Alcantar-Lopez, L. (2013). A USANS/SANS study of the accessibility of pores in the Barnett Shale to methane and water. *Energy & Fuels*, *27*(2), 772–779. https://doi.org/10.1021/ef301859s

Sabine, T. M., & Bertram, W. K. (1999). The use of multiple-scattering data to enhance small-angle neutron scattering experiments. *Acta Crystallographica Section A Foundations of Crystallography*, 55(3), 500–507. https://doi.org/10.1107/S0108767398013543

Sakurovs, R., Koval, L., Grigore, M., Sokolova, A., Ruppert, L. F., & Melnichenko, Y. B. (2017). Nanometre-sized pores in coal: Variations between coal basins and coal origin. *International Journal of Coal Geology*, *186*, 126-134. https://doi.org/10.1016/j.coal.2017.11.010

Thomas, J. J., Valenza, J. J., Craddock, P. R., Bake, K. D., & Pomerantz, A. E. (2014). The neutron scattering length density of kerogen and coal as determined by CH_3OH/CD_3OH exchange. *Fuel*, *117*(PART A), 801–808. https://doi.org/10.1016/j.fuel.2013.09.075

Chapter 5: Conclusions

This dissertation presents case studies of applying (U)SANS and MICP techniques to investigate petrophysical properties of rock samples in unconventional oil/gas reservoirs. Combined (U)SANS and MICP techniques yield a comprehensive pore structure (including both pore body and pore throat) over a wide pore length range from micrometer scale (>50 μm) to nanometer scale (minimum 1 nm). Assisted with SEM imaging techniques, as well as XRD and TOC analyses, pore types and their relationships with surrounding rock compositions (minerals or organic matters) are investigated.

Results from Chapter 2 and Chapter 3 showed that mineral pores are the primary contributors to the total porosity and are mostly well connected in the pore system. OM (organic matter)-hosted pores vary along with organic richness and thermal maturity, but typically have a large proportion of micropores (<2 nm) and mesopores (2-50 nm). Nano-scale pore throats play an important role in connecting multi-sized pore bodies. In general, macropores (> 50 nm) dominate pore systems, but a large fraction of total pore volume is associated with pores (either macropores or micro-/mesopores) interconnected by pore-throats smaller than 50 nm.

Chapter 4 showed the application of contrast matching method in combined SANS and USANS measurements which successfully characterized multiscale pore structure and wettability in studied shale samples. The quantification of fluid-accessible porosity and comparison with total porosity using different wetting fluids provides a unique way of seeing wettability from μm-scale to nm-scale.

Overall, this study proves the combined MICP and (U)SANS, assisted with XRD, TOC, and SEM imaging techniques, to be an effective way of characterizing pore structure over multiple scales and investigating relationships between pore types and rock compositions. The contrast

matching approach employed in (U)SANS measurements could be a very useful tool for quantifying fluid-wet pores for shales and providing invaluable insights to hydrocarbon storage and oil/gas recovery.